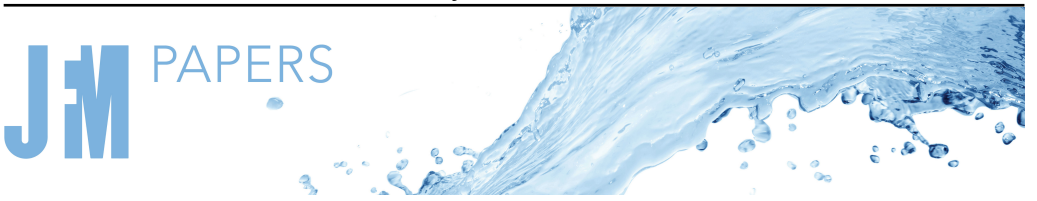
J. Fluid Mech. (2026), *vol.* 1041, A7, doi:10.1017/jfm.2026.11866



Swelling-induced flow evolution in shallow compliant microchannels

Kunal Kumar[1] **and Suman Chakraborty**[1]

[1]Department of Mechanical Engineering, Indian Institute of Technology Kharagpur, Kharagpur 721302, India

Corresponding author: Suman Chakraborty, suman@mech.iitkgp.ac.in

(Received 13 January 2026 UTC; revised 27 June 2026 UTC; accepted 30 June 2026 UTC)

Fluid transport through compliant microchannels is widely observed in both natural and engineered systems, including the transport of nutrients through xylem, mechano-chemically sensitive valves, hydrogel-based drug delivery systems and filter-paper-based diagnostic kits. In such flows, the two-way coupled interaction between fluid stresses and compliance of the bounding walls gives rise to a rich flow dynamics. These soft solid walls can absorb fluid and swell, and the resulting coupling between swelling kinetics and wall compliance further complicates the flow evolution, which can be observed in water flow through hydrogel microchannels or toluene flow through polydimethylsiloxane microchannels. Here, we develop a mathematical framework to investigate the spatio-temporal evolution of a Newtonian fluid flowing through a shallow rectangular microchannel bounded by soft, swelling walls. Using lubrication approximations, we derive a nonlinear diffusion equation for fluid pressure and channel height, which reveals a non-monotonic flow dynamics arising from the competition between swelling-induced collapse and fluid-pressure-induced restraint. A simplified analytical solution of the nonlinear diffusion equation, validated through fully coupled numerical simulations, identifies distinct regimes of flow evolution, and captures the transition from swelling-dominated to fluid-pressure-dominated behaviour, governed by the interplay between the swelling ratio and wall compliance. These results elucidate non-intuitive, yet fundamental flow responses in swelling, compliant channels, and highlight their implications for passive flow generation and flow control via mechano-chemical interactions.

Key words: microfluidics

© The Author(s), 2026. Published by Cambridge University Press. This is an Open Access article, distributed under the terms of the Creative Commons Attribution licence (https://creativecommons.org/licenses/by/4.0/), which permits unrestricted re-use, distribution and reproduction, provided the original article is properly cited.

https://doi.org/10.1017/jfm.2026.11866 Published online by Cambridge University Press

1. Introduction

Fluid flow through microchannels offers a wide range of possibilities to control and manipulate transport at very low flow rates ($\sim \mu$l/ min), where viscous forces dominate and the fluid flow interacts with mechanical properties of bounding walls (Squires & Quake 2005; Bruus 2011; Mehboudi & Yeom 2019; Park *et al.* 2021; Kramer & Modes 2023). These properties make microfluidic platforms suitable for biochemical, lab-on-a-chip and soft microfluidic devices, which can be used to generate controlled droplets at high throughput, facilitating passive mixing, sorting and drug discovery (Chakraborty 2010; Raj *et al.* 2016; Koldaeva *et al.* 2022). In many of these systems, the microchannels are fabricated from soft materials such as polydimethylsiloxane (PDMS) or hydrogels, whose mechanical compliance allows the channel walls to deform in response to fluid stress (Xia & Whitesides 1998; Raj *et al.* 2023; Kawara *et al.* 2023). This compliance enables closer emulation of biological transport processes, such as peristaltic flow in blood vessels and nutrient transport through micro- and nanopores (Heil *et al.* 2011; Meigel *et al.* 2018; Bhattacharyya *et al.* 2023). More broadly, soft substrates including hydrogels and filter papers support fluid transport through a combination of mechanical deformation and chemical interaction with the fluid, giving rise to flow behaviour that can depart markedly from that in rigid channels and exhibits a non-intuitive dynamics (Louf *et al.* 2020; Velde *et al.* 2024; Polygerinos *et al.* 2017; Xu *et al.* 2020).

Fluid flow through soft channels is accompanied by deformation of the bounding walls driven by fluid pressure, which in turn feeds back on the flow rate (Duprat *et al.* 2015; Karan *et al.* 2021; Christov 2022; M *et al.* 2019). This two-way fluid-structure coupling gives rise to a nonlinear relationship between flow rate and pressure drop ($q - \Delta p$), enabling passive flow regulation in compliant microfluidic systems (Christov *et al.* 2018; Raj *et al.* 2018; Box *et al.* 2020). A number of theoretical and analytical studies have characterised this behaviour for various geometries, including thick- and thin-walled rectangular and cylindrical channels, using various constitutive descriptions for both the solid and the fluid (Elbaz & Gat 2014, 2016; Raj & Sen 2016; Raj *et al.* 2017; Wang & Christov 2021). In these models, the local channel deformation is expressed solely as a function of fluid pressure, reflecting a purely mechanical forcing (Shidhore & Christov 2018; Wang & Christov 2019; Anand & Christov 2021). As a result, such formulations are not suited for describing flow evolution in channels bounded by soft, swelling walls, where deformation arises from coupled mechano-chemical interactions between the fluid and the solid (Dangla *et al.* 2010; Kim *et al.* 2014).

During swelling, a solid absorbs fluid and enlarges, driven by the chemical potential or osmotic pressure differences within the material (Li & Tanaka 1990; Yoon *et al.* 2010). This absorption and the movement of the walls during swelling directly influences the flow in the channel, altering the local flow velocity (Seo *et al.* 2019). In porous substrates, such as cellulose-based filter papers, swelling can significantly modify fluid transport, affecting reaction kinetics (Masoodi *et al.* 2010; Chang *et al.* 2020). Swelling can also interact with flow instabilities, for example tuning droplet formation through the Rayleigh–Plateau mechanism in co-flow set-ups (González-Estefan *et al.* 2019). While these phenomena demonstrate the effect of swelling on flow, the coupled effect of wall compliance and swelling in microchannels remains largely unexplored. This gap motivates a mechanistic study of how swelling-induced channel collapse competes with pressure-driven restraint to shape non-monotonic flow evolution.

During flow of an absorbable fluid through a channel bounded by soft walls, the fluid may diffuse into the polymeric matrix of the solid due to a gradient in the chemical potential (Duprat 2022; Velde *et al.* 2023; Yoon *et al.* 2010). The absorbed fluid generates

https://doi.org/10.1017/jfm.2026.11866 Published online by Cambridge University Press

internal stresses that deform the solid, a process known as swelling, which in turn modifies the local flow rate along the channel length (Velde *et al.* 2025). Previous studies have often employed empirical expressions to describe swelling-induced deformation, such as the linear time dependence: $r(t) = r_0 - at$, where r_0 is the initial size, and a is the rate of change with time (Masoodi *et al.* 2010; Chang *et al.* 2020; Patari *et al.* 2023). While such formulations capture time-dependent changes in channel dimensions, they conflict with diffusion theory, which predicts a decay in the swelling rate over time, upon absorption. Theoretical models based on chemical-potential-driven absorption, coupled with Biot's poroelasticity, demonstrate that the swelling kinetics follow an exponential decay ($\mathrm{d}r/\mathrm{d}t \propto e^{-t}$), a behaviour observed experimentally across materials including textiles, hydrogels in water and PDMS in non-polar solvents (Soltane *et al.* 2013; Keshmiri *et al.* 2019; Chang *et al.* 2020). This exponentially decaying rate law defines a characteristic swelling time scale and an amplitude, determined by the mechano-chemical properties of the fluid–solid pair. Chang *et al.* (2020) used this framework to model capillary radius evolution during water imbibition in hydrogel-coated capillaries, and validated the mathematical model against experiments, illustrating how swelling can progressively reduce capillary radius until complete collapse occurs.

For soft-walled channels, swelling-induced collapse increases the fluid pressure under a flow-rate-controlled inlet, which can counteract further closure of the channel, depending on the walls' compliance and swelling properties. This competition between the two stresses – swelling and fluid pressure, in which the former augments the latter, while the latter opposes the former – may give rise to an intriguing spatio-temporal evolution of flow profile along the channel. The relative strength of these two effects depends critically on the flow conditions, channel geometry and the mechano-chemical properties of both the fluid and the solid.

In this work, we study the incompressible flow of a Newtonian fluid through a shallow rectangular microchannel (width $\gg$ height) bounded by soft solids that can swell upon fluid absorption. The system is relevant to both biological and microfluidic contexts, where flow rates are sufficiently low to characterise as low-Reynolds-number hydrodynamics (Kramer & Modes 2023; Raj *et al.* 2023). We employ the lubrication approximation to derive unsteady governing equations for the fluid flow through the compliant swelling channel (Panda *et al.* 2009; Inamdar *et al.* 2020; Martínez-Calvo *et al.* 2020). The net channel deformation depends on the combined effect of swelling kinetics and fluid pressure. For the small swelling ratios considered in this study, we adopt a linear swelling model based on chemical-potential-driven fluid diffusion (Yoon *et al.* 2010; Bouklas & Huang 2012). For larger swelling ratios, the presented linear model needs to be replaced with nonlinear swelling models (Chen *et al.* 2020; Webber & Worster 2023). Combining the lubrication-approximation-based fluid flow governing equation with the spatio-temporally varying deformation yields a nonlinear diffusion equation governing channel height (or fluid pressure) (Martínez-Calvo *et al.* 2020). We validate this model with fully coupled direct numerical simulations of the Navier–Stokes equations for the fluid and Navier equations for solid, with fluid diffusion into the solid governed by Fick's and Darcy's laws. For weak compliance, we also derive a simplified analytical solution. Using this framework, we explore how swelling and fluid pressure shape the evolution of flow patterns and demonstrate the transition from swelling-dominated to fluid-pressure-dominated regimes, determined by the relative strength of swelling-induced collapse and pressure-mediated restraint.

The paper is organised as follows: the flow configuration is described in § 2. In § 3, we present the mathematical framework for fluid flow, using the lubrication approximation, followed by the modelling of the solid's deformation. By combining these

https://doi.org/10.1017/jfm.2026.11866 Published online by Cambridge University Press

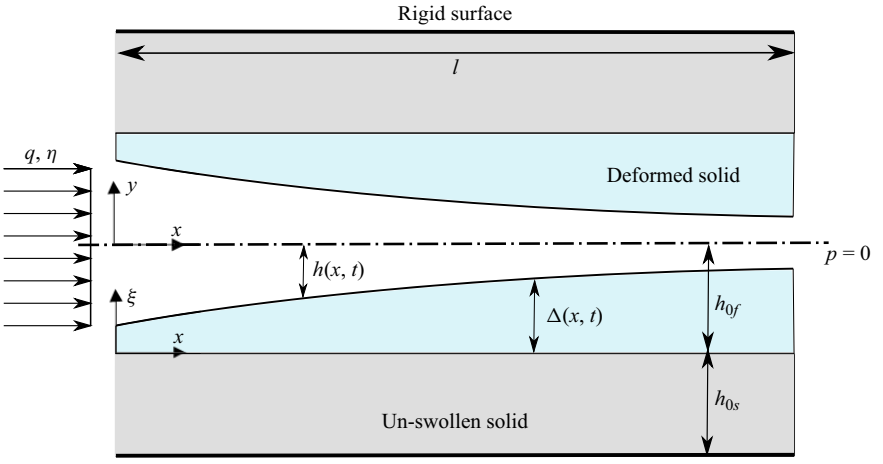


Figure 1. Schematic of the flow domain illustrating the deformation of the solid due to the combined effect of swelling and fluid pressure, subject to a constant inlet flow rate q_0.

two frameworks, we derive the final governing equation that describes the coupled physics, along with a simplified analytical solution for weak compliance. In § 4, we outline the set-up for fully coupled direct numerical simulation using the COMSOL Multiphysics platform. In § 5, we present the results, including validation of the mathematical model and approximate analytical solution with the numerical simulations. Finally, in § 6, we summarise the main findings.

2. Flow configuration

We consider incompressible, low-Reynolds-number flow of a Newtonian fluid in a two-dimensional parallel-plate channel of undeformed half-height h_{0f} and length l, subject to a constant inlet flow rate $q(x = 0, t) = q_0$, exiting at outlet pressure $p = 0$, as illustrated in figure 1. The channel is bounded by soft polymeric layers of thickness h_{0s}, which can swell upon fluid absorption, and deform the channel spatio-temporally. The soft solid layers are bonded to rigid surfaces, which impose a zero-displacement constraint at the outer boundaries.

We use a Cartesian coordinate system (x, y) for the fluid, with x-axis along the channel centreline, and the velocity field is denoted by $\boldsymbol{v} = (v_x, v_y)$. A separate Cartesian coordinate (x, ξ) aligned with the surface of the solid, as shown in figure 1, is used to describe the solid deformation, and to denote the deformation field $\boldsymbol{u} = (u_x, u_\xi)$. The deformation of the solid surface along ξ, due to the combined effect of swelling and fluid pressure, is denoted by $\Delta(x, t)$, as illustrated in figure 1. This deformation reduces the local half-height available for the flow: $h(x, t) = h_{0f} - \Delta(x, t)$.

In this study, both the channel and solid layers are thin compared with their length, i.e. $h_{0f} \ll l$ and $h_{0s} \ll l$, justifying the use of lubrication approximation . We also limit the analysis to the small linear deformation regime $\Delta(x, t)/h_{0s} \lesssim 0.1$, as detailed in § 3.2.

3. Problem formulation

3.1. *Governing equation for flow: lubrication approximation*

We consider the unsteady flow of a Newtonian fluid through the two-dimensional channel, whose velocity field $\boldsymbol{v} = (v_x, v_y)$ is governed by the continuity and Navier–Stokes

https://doi.org/10.1017/jfm.2026.11866 Published online by Cambridge University Press

equations

$$\frac{\partial v_x}{\partial x} + \frac{\partial v_y}{\partial y} = 0, \tag{3.1a}$$

$$\rho_f \left[\frac{\partial v_x}{\partial t} + v_x \frac{\partial v_x}{\partial x} + v_y \frac{\partial v_x}{\partial y} \right] = -\frac{\partial p}{\partial x} + \eta \left(\frac{\partial^2 v_x}{\partial x^2} + \frac{\partial^2 v_x}{\partial y^2} \right), \tag{3.1b}$$

$$\rho_f \left[\frac{\partial v_y}{\partial t} + v_x \frac{\partial v_y}{\partial x} + v_y \frac{\partial v_y}{\partial y} \right] = -\frac{\partial p}{\partial y} + \eta \left(\frac{\partial^2 v_y}{\partial x^2} + \frac{\partial^2 v_y}{\partial y^2} \right), \tag{3.1c}$$

where ρ_f and η are the fluid's density and viscosity, respectively, and p is the fluid pressure. The x-component of fluid velocity satisfies the no-slip condition at the walls, i.e. $v_x = 0$ at $y = \pm h(x, t)$ and symmetry at the centreline, i.e. $\partial v_x/\partial y = 0$ at $y = 0$. Since, the fluid can penetrate into the solid upon absorption, the net wall-normal velocity at the wall is the algebraic sum of the absorption velocity and wall deformation rate, given by: $v_y = \pm(v_{abs} + \partial h/\partial t)$ at $y = \pm h(x, t)$, where v_{abs} is the absorption velocity. At the inlet, the mean velocity is $v_{x,m} = q/(2h(0, t))$, and at the outlet, $p = 0$.

We non-dimensionalise the variables using appropriate scales: $X = (x/l)$, $Y = (y/h_{0f})$, $V_X = (v_x/(q/h_{0f}))$, $V_Y = (v_y/(\epsilon q/h_{0f}))$, $P = (p/p_0)$ and $T = (t/t_s)$, where p_0 is pressure scale, t_s is the characteristic swelling time scale and $\epsilon = (h_{0f}/l) \ll 1$ is the aspect ratio of the channel. The pressure scale p_0 is obtained by equating the scales of axial pressure gradient and the transverse viscous diffusion term on the right-hand side of (3.1*b*), yielding $p_0 = lq\eta/h_{0f}^3$. Using these scalings, the set of governing equations (3.1*a*–*c*) can be written in the non-dimensional form as

$$\frac{\partial V_X}{\partial X} + \frac{\partial V_Y}{\partial Y} = 0, \tag{3.2a}$$

$$ReSt\frac{\partial V_X}{\partial T} + ReV_X\frac{\partial V_X}{\partial X} + ReV_Y\frac{\partial V_X}{\partial Y} = -\frac{\partial P}{\partial X} + \epsilon^2\frac{\partial^2 V_X}{\partial X^2} + \frac{\partial^2 V_X}{\partial Y^2}, \tag{3.2b}$$

$$\epsilon ReSt\frac{\partial V_Y}{\partial T} + \epsilon ReV_X\frac{\partial V_Y}{\partial X} + \epsilon ReV_Y\frac{\partial V_Y}{\partial Y} = -\frac{1}{\epsilon}\frac{\partial P}{\partial Y} + \epsilon^3\frac{\partial^2 V_Y}{\partial X^2} + \epsilon\frac{\partial^2 V_Y}{\partial Y^2}, \tag{3.2c}$$

where $Re = \epsilon Re^* \ll 1$ is the reduced Reynolds number, such that $Re^* = \rho_f q/\eta$ is the Reynolds number. Another key dimensionless number appearing in the set of non-dimensional equations is the Strouhal number, which is defined as the ratio of flow time scale ($t_f = lh_{0f}/q$) to swelling time scale (t_s), given by $St = (t_f/t_s) = (lh_{0f}/qt_s)$. The order of magnitude analysis reduces (3.2*c*) to $(\partial P/\partial Y) \approx 0 + O(\epsilon^2)$ for $\epsilon \ll 1$. This implies that the fluid pressure remains uniform across the channel height, and varies as $P \approx P(X, T)$. Similarly, (3.2*b*) can be written up to leading-order terms

$$\frac{\partial P}{\partial X} = \frac{\partial^2 V_X}{\partial Y^2}. \tag{3.3}$$

It should be noted that the unsteady term in the non-dimensionalised X-momentum equation, i.e. $ReSt(\partial V_X/\partial T)$, can be neglected for microfluidic flow because $ReSt \ll 1$. This quasi-steady assumption, however, breaks down for $St \gg 1$, where the inertial time-derivative term in (3.2*b*) become significant. In the present study, we consider $St \lesssim O(1)$, representing flow and swelling time scales of a similar order, which is consistent with the upper limit for typical microfluidic set-ups (see table 2). After order of magnitude analysis, the leading-order equations, (3.2*a*) and (3.3) do not contain an

https://doi.org/10.1017/jfm.2026.11866 Published online by Cambridge University Press

explicit time-derivative term, indicating a quasi-steady flow. Importantly, this quasi-steady behaviour arises from the low-Reynolds-number characteristic of microchannels, rather than the absolute time scales of flow and swelling. Consequently, any temporal variations in the flow field are imposed solely through the boundary conditions.

The spatio-temporally varying flow rate can be obtained by integrating (3.2*a*) along the half-height of the domain (due to symmetry) from $Y = 0$ to $Y = H(X, T)$, where $H(X, T) = h(x, t)/h_{0f}$, yielding

$$\frac{1}{2}\frac{\partial Q(X, T)}{\partial X} + V_Y\,(X, Y = H, T) = 0, \tag{3.4}$$

with $Q(X, T) = 2\int_0^{H(X,T)} V_X \mathrm{d}Y$. While integrating (3.2*a*), we have used Leibniz integral rule with the no-slip boundary condition at the wall, i.e. $V_X(X, Y = H, T) = 0$, and symmetry at the centreline $V_Y(X, Y = 0, T) = 0$. For weakly swelling materials, the swelling rate is typically proportional to the rate of fluid absorption, i.e. $v_{abs} \propto \partial h_s/\partial t$ (Chang *et al.* 2022), therefore, the net fluid velocity along the Y-direction at the wall can be expressed as

$$V_Y\,(X, Y = H, T) = (1 - \alpha)\frac{\partial H}{\partial T}, \tag{3.5}$$

where α is the ratio of absorption rate to swelling rate. For $\alpha > 1$, absorption rate into the solid exceeds the swelling rate, so $V_Y(X, Y = H, T) > 0$, as the channel gap reduces $\partial H/\partial T < 0$, and *vice versa*. Substituting (3.5) into (3.4) gives

$$\frac{1}{2}\frac{\partial Q(X, T)}{\partial X} + (1 - \alpha)\frac{\partial H}{\partial T} = 0, \tag{3.6}$$

which represents the mass conservation equation in integral form, and can also be derived from the Reynolds transport theorem.

The axial velocity profile V_X at a given streamwise location X is obtained by integrating (3.3) twice with respect to Y, subject to: (i) symmetry at the centreline: $(\partial V_X/\partial Y)_{Y=0} = 0$, and (ii) a no-slip condition at the wall: $V_X(X, Y = H, T) = 0$, which yields the parabolic velocity profile

$$V_X\,(X, Y, T) = -\frac{1}{2}\frac{\partial P(X, T)}{\partial X}\left(H^2 - Y^2\right). \tag{3.7}$$

Integrating (3.7) along the channel height gives the local flow rate

$$Q(X, T) = -\frac{2}{3}H^3(X, T)\frac{\partial P}{\partial X}. \tag{3.8}$$

Substituting (3.8) into the mass conservation relation (3.6) leads to

$$(1 - \alpha)\frac{\partial H(X, T)}{\partial T} = \frac{1}{3}\frac{\partial}{\partial X}\left[H^3(X, T)\frac{\partial P}{\partial X}\right]. \tag{3.9}$$

The prefactor $(1 - \alpha)$ quantifies the relative importance of swelling-induced deformation compared with fluid absorption, and therefore, governs whether the flow rate increases or decreases along the channel length, as implied by (3.6). To close (3.9), we need to specify the relation linking the channel height $H(X, T)$ and fluid pressure $P(X, T)$, via swelling kinetics. This enables (3.9) to be cast as a nonlinear diffusion equation in either $H(X, T)$ or $P(X, T)$, subject to appropriate boundary conditions.

https://doi.org/10.1017/jfm.2026.11866 Published online by Cambridge University Press

3.2. *Deformation due to swelling and fluid pressure*

The swelling kinetics of polymeric solids have been extensively studied by combining fluid diffusion into the porous network with the resulting deformation using the theory of poroelasticity (Tanaka & Fillmore 1979; Li & Tanaka 1990; Liu *et al.* 2013). Earlier models employed linear poroelasticity, assuming strain-independent material properties (Yoon *et al.* 2010; Drozdov *et al.* 2014). However, for large swelling ratios ($\sim$100 %), this assumption fails due to significant changes in material properties, such as permeability and elastic modulus. Several nonlinear models have been developed to capture swelling kinetics under such conditions (Bouklas & Huang 2012; Webber & Worster 2023). Linear models, while accurate for predicting deformation over time for moderate swelling ratios ($\sim$50 %), cannot reliably predict stress, limiting their applicability to low swelling ratios ($\lesssim$20 %). In the present study, we consider weakly swelling materials, with swelling ratios $\sim$10 %, allowing the use of a linear swelling model, and neglecting changes in material properties upon deformation. For large swelling ratios, nonlinear models are required, which is beyond the scope of the present work (Kvick *et al.* 2017).

The coupling between the fluid flow and solid mechanics involves three distinct time scales: the elastic deformation time scale $t_d \sim \sqrt{\rho_s h_{0s}^2/E}$, the convective flow time scale $t_f \sim l h_{0f}/q$ and the swelling time scale t_s. For the characteristic material properties and dimensions considered in this study (see table 1), the elastic time scale is approximately $t_d \sim O(10^{-4})s$, whereas the flow and swelling time scales are significantly larger, $t_f, t_s \gtrsim 10\,s$. Given that $t_d \ll t_f$ and $t_d \ll t_s$, the solid reaches mechanical equilibrium much faster than the time required for significant fluid transport or swelling to occur. Consequently, we assume the elastic response of the channel walls to the fluid pressure is instantaneous.

Upon deformation, the infinitesimal strain tensor s_{ij} in the solid is related to the displacement field $\boldsymbol{u}$ as

$$s_{ij} = \frac{1}{2}\left(\frac{\partial u_i}{\partial x_j} + \frac{\partial u_j}{\partial x_i}\right), \tag{3.10}$$

where u_m denotes displacements in mth-direction, $m = x, y$. Deformation of the solid leads to storage of the free energy, comprising elastic energy and the chemical potential energy associated with the absorbed fluid. The corresponding variation of the Helmholtz free energy may be written as (Yoon *et al.* 2010)

$$\delta W = \sigma_{ij}\delta s_{ij} + (\mu - \mu_0)\,\delta c, \tag{3.11}$$

where $\mu(x_i, x_j, t)$ is the chemical potential of the absorbed fluid, μ_0 is its reference value, and c denotes the fluid concentration.

The swelling-induced volumetric strain corresponds to the volume of absorbed fluid, and is therefore proportional to the concentration change, such that $\delta s_{kk} = a\Omega\delta c$, where a is a proportionality constant, and Ω is the molecular volume of the fluid. Substituting this relation into (3.11) and differentiating with respect to the strain yields the stress tensor

$$\sigma_{ij} = \frac{\delta W}{\delta s_{ij}} - \frac{(\mu - \mu_0)}{a\Omega}\delta_{ij}, \tag{3.12}$$

where δ_{ij} is the Kronecker delta. Within the framework of linear elasticity, the elastic free energy density is given by $W = G[s_{ij}s_{ij} + (\nu/(1-2\nu))s_{kk}^2]$, where G is the shear modulus, and ν is Poisson's ratio. Substituting into (3.12) yields the relation for the stress

https://doi.org/10.1017/jfm.2026.11866 Published online by Cambridge University Press

tensor

$$\sigma_{ij} = 2G\left[s_{ij} + \frac{\nu}{1-2\nu}s_{kk}\delta_{ij}\right] - \frac{(\mu-\mu_0)}{a\Omega}\delta_{ij}. \tag{3.13}$$

The material properties of the solid are assumed to remain constant throughout the swelling, consistent with the assumption of weak swelling. The quasi-static mechanical equilibrium of the solid is then governed by Cauchy's momentum equation

$$\frac{\partial \sigma_{ij}}{\partial x_j} = 0. \tag{3.14}$$

Since the in-plane dimensions of the solid are much larger than the thickness, i.e. $h_{0s} \ll l$, the fluid absorption and subsequent swelling occur predominantly along the thickness, i.e. the $\pm\xi$-direction. Consequently, the in-plane strain remains negligible, i.e. $s_{xx} \ll s_{\xi\xi}$. Therefore, the relevant stress balance equation along the ξ direction is given by

$$\frac{\partial \sigma_{\xi x}}{\partial x} + \frac{\partial \sigma_{\xi\xi}}{\partial \xi} = 0. \tag{3.15}$$

Using the characteristic deformation scale u_c along the ξ-direction, the stress components scale as $\sigma_{x\xi} \sim Gu_c/l$ and $\sigma_{\xi\xi} \sim Gu_c/h_{0s}$. Substitution into (3.15) shows that the first term scales as u_c/l^2, while the second term varies as u_c/h_{0s}^2. Since $h_{0s} \ll l$, the stress balance equation reduces to

$$\frac{\partial \sigma_{\xi\xi}}{\partial \xi} = 0. \tag{3.16}$$

The solid surface in contact with the fluid experiences a normal compressive stress equal to the fluid pressure, such that $\sigma_{\xi\xi}(\xi = 0) = -p$. Using this boundary condition in (3.16) implies $\sigma_{\xi\xi} = -p$ throughout the solid thickness. Substituting this condition into (3.13) leads to $\sigma_{\xi\xi} = (\lambda + 2G)s_{\xi\xi} - ((\mu-\mu_0)/a\Omega)$, which upon re-arrangement, yields

$$s_{\xi\xi} = \frac{\partial u_\xi}{\partial \xi} = -\frac{p}{\lambda+2G} + \frac{1}{\lambda+2G}\frac{\mu-\mu_0}{a\Omega}, \tag{3.17}$$

where $\lambda = (2\nu/(1-2\nu))G$ is Lamé's first parameter. Equation (3.17) shows that the total strain can be decomposed as $s_{\xi\xi} = s_p + s_s$, where s_p arises from fluid pressure, and s_s from swelling. The swelling-induced strain is thus

$$s_s = \frac{\partial u_s}{\partial \xi} = \frac{1}{\lambda+2G}\frac{\mu-\mu_0}{a\Omega}. \tag{3.18}$$

The diffusion of fluid within the solid is governed by the conservation equation

$$\frac{\partial c}{\partial t} + \frac{\partial J_\xi}{\partial \xi} = 0, \tag{3.19}$$

where the flux is driven by the chemical potential gradient $J_\xi = -(K/\eta\Omega^2)(\partial\mu/\partial\xi)$, and K is the permeability. Combining (3.18) and (3.19) with the relation $\delta s_s = a\Omega\delta c$ yields a diffusion equation for the swelling-induced strain

$$\frac{\partial s_s}{\partial t} = D\frac{\partial^2 s_s}{\partial \xi^2}, \tag{3.20}$$

where $D = (Ka^2(\lambda+2G))/\eta$ is the effective diffusion coefficient. Equation (3.20) is subject to the initial condition $s_s(\xi, t=0) = 0$. At the fluid–solid interface $\xi = 0$,

https://doi.org/10.1017/jfm.2026.11866 Published online by Cambridge University Press

the chemical potential remains constant at $\mu = \overline{\mu}$, which implies $s_s = (1/(\lambda + 2G))((\overline{\mu} - \mu_0)/a\Omega)$. At the bottom surface $\xi = -h_{0s}$, which is rigid and impermeable, the no-flux condition yields $\partial s_s/\partial \xi = 0$. Solving the linear diffusion (3.20) subject to these conditions yields

$$s_s = \frac{1}{\lambda + 2G}\frac{\overline{\mu} - \mu_0}{a\Omega}\left[1 + \sum_{n=0}^{\infty}\frac{4}{\pi(2n+1)}\exp\left\{-(2n+1)^2\frac{t}{t_s}\right\}\sin\left\{\frac{(2n+1)\pi}{2h_{0s}}\xi\right\}\right], \tag{3.21}$$

where $t_s = 4h_{0s}^2/\pi^2 D$ is the characteristic swelling time scale of the solid, which is similar to the diffusion time scale $\propto$ length^2/diffusion coefficient. Equation (3.21) can be integrated along the thickness to obtain the displacement field in the solid due to swelling, imposing zero displacement at the rigid surface, i.e. $u_s(\xi = -h_{0s}, t) = 0$, yielding

$$u_s = \frac{1}{\lambda + 2G}\frac{\overline{\mu} - \mu_0}{a\Omega}\left[(\xi + h_{0s}) - \sum_{n=0}^{\infty}\frac{8h_{0s}}{\pi^2(2n+1)^2}\exp\left\{-(2n+1)^2\frac{t}{t_s}\right\}\cos\left\{\frac{(2n+1)\pi}{2h_{0s}}\xi\right\}\right]. \tag{3.22}$$

The swelling amplitude can be obtained by evaluating the surface displacement at $\xi = 0$ in the long-time limit $t \to \infty$, resulting in

$$\Delta_{s,\infty} = \frac{h_{0s}}{\lambda + 2G}\frac{\overline{\mu} - \mu_0}{a\Omega}, \tag{3.23}$$

which represents the maximum swelling magnitude. Using (3.23) to normalise (3.22), the instantaneous swelling magnitude can be expressed in the dimensionless form as

$$\frac{\Delta_s}{\Delta_{s,\infty}} = 1 - \sum_{n=0}^{\infty}\frac{8}{\pi^2(2n+1)^2}\exp\left[-(2n+1)^2 T\right] \equiv \mathcal{F}_n(T), \tag{3.24}$$

where $T = t/t_s$ is the dimensionless time. Several experimental studies of swelling kinetics approximate the transient swelling response using a single exponential form

$$\frac{\Delta_s(T)}{\Delta_{s,\infty}} = 1 - \exp(-T), \tag{3.25}$$

which captures the long-time behaviour.

We compare the truncated series solution given by (3.24) for different values of n, as well as the single exponential approximation given by (3.25), with results from direct numerical simulations performed using COMSOL Multiphysics, as shown in figure 2. The details of the simulation methodology are provided in § 4. The single exponential model given by (3.25) systematically underpredicts the swelling magnitude at early time, with a maximum deviation of ∼0.14, although it converges towards the simulation results at later times. In contrast, the series solution, (3.24), exhibits better agreement over the entire time range, despite the presence of initial truncation error $\mathcal{F}_n(T = 0) \neq 0$. Increasing n reduces this error, bringing $\mathcal{F}_n(T = 0)$ closer to its ideal value of 0. For $n = 5$, the deviation is less than 3 %, and hence we adopt $\Delta_s(T)/\Delta_{s,\infty} = \mathcal{F}_5(T)$ to estimate the swelling magnitude in subsequent analyses.

The deformation induced by fluid pressure is obtained by integrating the corresponding strain component from (3.17), $s_p = -(p/(\lambda + 2G))$. Defining the compliance parameter $\varrho = p_0/(\lambda + 2G)$ as the ratio between the viscous pressure scale and the elastic stiffness of the solid, the strain due to fluid pressure simplifies to $s_p = (\partial u_p/\partial \xi) = -P\varrho$, where P is dimensionless fluid pressure. Imposing the boundary condition of zero displacement at the rigid base, i.e. $u_p = 0$ at $\xi = -h_{0s}$, the deformation of the fluid–solid interface at

https://doi.org/10.1017/jfm.2026.11866 Published online by Cambridge University Press

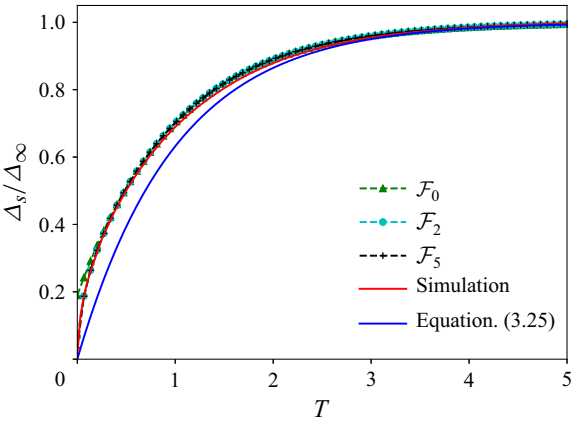


Figure 2. Temporal evolution of the normalised swelling magnitude Δ_s/Δ_∞, comparing the truncated series solution $\mathcal{F}_n(T)$ given by (3.24) for different values of n, the single exponential approximation given by (3.25), and results from direct numerical simulations.

$\xi = \Delta_s$ due to fluid pressure is given by

$$\Delta_p = -P\varrho\,(\Delta_s(T) + h_{0s})\,. \tag{3.26}$$

Combining (3.24) and (3.26), the total deformation at any streamwise location, $\Delta(X, T) = \Delta_s + \Delta_p$, is given by

$$\Delta(X, T) = \Delta_s(T) - \varrho P(X, T)\,(\Delta_s(T) + h_{0s})\,. \tag{3.27}$$

The half-height of the deformed channel can be obtained by subtracting the net solid deformation from the initial height, which, in dimensionless form, becomes

$$H(X, T) = 1 - \frac{\Delta(X, T)}{h_{0f}} = A(T) + B(T)P(X, T), \tag{3.28}$$

where $A(T) = 1 - (\Delta_s/h_{0f}) = 1 - \beta\mathcal{F}_n(T)$ and $B(T) = \varrho((\Delta_s + h_{0s})/h_{0f}) = \varrho(\beta\mathcal{F}_n(T) + \varkappa)$. Here, $\beta = \Delta_{s,\infty}/h_{0f}$ measures the extent of channel collapse due to swelling, and $\varkappa = h_{0s}/h_{0f}$ is the ratio of solid thickness to initial half-height of the channel. These parameters govern the relative influence of swelling-induced expansion and fluid-pressure-induced compression, which act in opposing directions to determine the instantaneous channel geometry.

3.3. *Diffusion equation for channel height*

In (3.28), we express the spatio-temporal variation in half-channel height $H(X, T)$ as a linear function of $P(X, T)$. Rearranging (3.28), the fluid pressure can be written in terms of $H(X, T)$ as

$$P(X, T) = \frac{H(X, T) - A(T)}{B(T)}, \tag{3.29}$$

which, upon substitution in (3.9), yields a nonlinear diffusion equation governing the evolution of channel height

$$(1 - \alpha)\frac{\partial H(X, T)}{\partial T} = \frac{1}{3}\frac{\partial}{\partial X}\left[\frac{H^3(X, T)}{B(T)}\frac{\partial H(X, T)}{\partial X}\right]. \tag{3.30}$$

https://doi.org/10.1017/jfm.2026.11866 Published online by Cambridge University Press

Equation (3.30) needs to be solved subject to the following initial and boundary conditions:

$$\text{initial condition}: \quad H(X, 0) = 1, \tag{3.31a}$$

$$\text{inlet (flow-rate controlled)}: \quad \frac{\partial H(0, T)}{\partial X} + \frac{3B(T)}{2H^3(0, T)} = 0, \tag{3.31b}$$

$$\text{outlet (zero pressure)}: \quad H(X = 1, T) = A(T). \tag{3.31c}$$

Here, the inlet boundary condition is obtained by combining (3.6), (3.8) and (3.29), for a constant imposed inlet flow rate $Q(X = 0, T) = 1$.

We solve this nonlinear diffusion equation (3.30) subject to the initial condition (3.31*a*) and the boundary conditions (3.31*b*–*c*) using the *LinearLUSolver* class of the *FiPy* package in Python. *FiPy* is a Python-based partial differential equation solver package based on the finite volume method. It discretises the governing equation over the computational mesh, resulting in a system of algebraic equations, which is solved using the lower–upper (LU) factorisation method by *LinearLUSolver*. We discretise the domain $X \in [0, 1]$ into 80 uniform grid cells, corresponding to grid size $\Delta X = 1/80$ to form one-dimensional linear cells. Time integration was performed using a uniform time step $\Delta T = 5 \times 10^{-3}$. At each time step, a maximum of 50 solver iterations was allowed, with a convergence tolerance of 10^{-4}.

3.4. *Analytical solution for $\varrho \ll 1$*

In the limit of a very small compliance ratio, $\varrho \ll 1$, the deformation induced by fluid pressure remains weak, implying $B(T) \ll 1$. Under this small deformation limit, the nonlinear diffusion equation (3.30) can be expanded to leading order in B, reducing it to an ordinary differential equation in X

$$\frac{\partial}{\partial X}\left[H^3 \frac{\partial H(X, T)}{\partial X}\right] = 3B(1 - \alpha)\frac{\mathrm{d}A(T)}{\mathrm{d}T}. \tag{3.32}$$

Equation (3.32) may alternatively be obtained by approximating $(\partial H(X, T)/\partial T) \approx (\mathrm{d}A(T)/\mathrm{d}T)$ in (3.6). This approximation neglects the contribution of fluid-pressure-induced deformation on the axial variation of the flow rate, which is justified when the swelling time scale t_s is large compared with the elastic response time of the solid. In this regime, axial variations in flow rate arise predominantly from swelling-induced displacement and fluid absorption.

Introducing the transformation $G(X, T) = H^4(X, T)$, (3.32) can be rewritten as

$$\frac{\partial^2 G(X, T)}{\partial X^2} = 12B(1 - \alpha)\frac{\mathrm{d}A(T)}{\mathrm{d}T}. \tag{3.33}$$

The corresponding initial and boundary conditions transform to

$$\text{initial condition}: \ : \quad G(X, 0) = 1, \tag{3.33a}$$

$$\text{inlet (flow-rate controlled)}: \quad \frac{\partial G(0, T)}{\partial X} + 6B(T) = 0, \tag{3.33b}$$

$$\text{outlet (zero pressure)}: \quad G(X = 1, T) = A^4(T). \tag{3.33c}$$

https://doi.org/10.1017/jfm.2026.11866 Published online by Cambridge University Press

We integrate the (3.33) twice with respect to X, and applying the conditions (3.33*a–c*) yields the analytical expression for the half-height of the channel

$$H(X,T)=\left[A^4(T)-6B(T)(1-\alpha)\frac{dA(T)}{dT}\left(1-X^2\right)+6B(T)\,(1-X)\right]^{\frac{1}{4}}. \tag{3.34}$$

At early times, $T\ll 1$, we have $B(T)=\varrho(\beta\mathcal{F}_n(T)+\varkappa)\sim\varrho\varkappa\ll 1$ and $A(T)\approx 1$, so that $H(X,T)\approx A(T)$, with the remaining terms in (3.34) being negligible. In contrast, at later times, $T\gg 1$, the ratio B/A^4 may become $O(10^{-1}-1)$ for sufficiently large ϱ and β. In this regime, the second and third terms on the right-hand side of (3.34), corresponding to fluid-pressure-induced deformation, become comparable to the swelling contribution represented by the first term. This behaviour arises from the sharp increase in fluid pressure upon channel collapse due to swelling, which can lead to substantial deformation of the compliant, swelling solid.

4. Fully coupled numerical simulation

4.1. *Governing equations*

The governing equations for the fluid are the continuity and momentum balance equations

$$\rho_f\nabla\cdot\boldsymbol{v}=0, \tag{4.1}$$

$$\rho_f\frac{\partial\boldsymbol{v_f}}{\partial t}+\rho_f\,(\boldsymbol{v}\cdot\nabla)\,\boldsymbol{v}=\nabla\cdot\left[-p\boldsymbol{I}+\eta\left(\nabla\boldsymbol{v}+(\nabla\boldsymbol{v})^T\right)\right], \tag{4.2}$$

where $\boldsymbol{v}$ is the fluid velocity vector, ρ_f is the density, η is the viscosity, p is the fluid pressure and $\boldsymbol{I}$ is the unit tensor.

The deformable solid is modelled as a linear elastic material, whose deformation is governed by the balance of linear momentum

$$\rho_s\frac{\partial^2\boldsymbol{u}}{\partial t^2}=\nabla\cdot(\boldsymbol{FS})^T+\boldsymbol{F}_V, \tag{4.3}$$

where $\boldsymbol{u}$ is the deformation field, ρ_s the solid density and $\boldsymbol{F}_V$ is the body force, which is neglected in the present study. The deformation gradient tensor $\boldsymbol{F}$ is defined as

$$\boldsymbol{F}=\boldsymbol{I}+\nabla\boldsymbol{u}. \tag{4.4}$$

The net strain tensor is written as

$$\boldsymbol{E}=\boldsymbol{E_{el}}+\boldsymbol{E_{sw}}=\frac{\boldsymbol{1}}{\boldsymbol{2}}\left(\boldsymbol{F^TF}-\boldsymbol{I}\right), \tag{4.5}$$

where $\boldsymbol{E_{el}}$ and $\boldsymbol{E_{sw}}$ denote elastic strain and contribution due to swelling, respectively. The swelling-induced strain remains proportional to the absorbed fluid concentration

$$\boldsymbol{E_{sw}}=\beta_h M_m(c-c_0), \tag{4.6}$$

where β_h is the swelling coefficient, M_m is the molar mass of the fluid and c_0 is the reference concentration in the solid, taken here as $c_0=0$. The second Piola–Kirchhoff stress tensor $\boldsymbol{S}$ is related to the Cauchy stress σ_s by

$$\boldsymbol{S}=\mathcal{J}\boldsymbol{F^{-1}\sigma_s F^{-T}}, \tag{4.7}$$

where $\mathcal{J}=\det(\boldsymbol{F})$. Assuming isotropic linear elasticity, the constitutive relation is given by the Saint Venant–Kirchhoff model, which extends Hooke's law to account for finite

https://doi.org/10.1017/jfm.2026.11866 Published online by Cambridge University Press

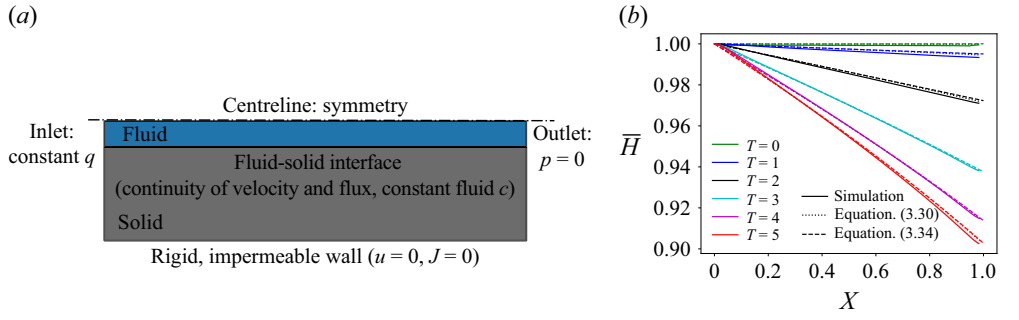


Figure 3. (*a*) Schematic of the computational domain used for simulations. (*b*) Comparison of the spatio-temporal evolution of the half-height of the channel, normalised by its inlet value at the corresponding time, $\overline{H}(X, T) = H(X, T)/H(0, T)$. Results obtained from the numerical solution of the nonlinear diffusion equation (3.30) and its approximate analytical solution (3.34) are compared with direct numerical simulations performed in COMSOL Multiphysics. Parameters: $\beta = 0.8$, $\varkappa = 8$, $\varrho = 1.5 \times 10^{-5}$.

deformations

$$\boldsymbol{S} = \lambda\,(\mathrm{tr}\boldsymbol{E})\,\boldsymbol{I} + 2G\boldsymbol{E}. \tag{4.8}$$

The evolution of absorbed fluid concentration within the solid is governed by Fickian diffusion

$$\frac{\partial c}{\partial t} = \boldsymbol{\nabla}\cdot(D_0\boldsymbol{\nabla}c)\,, \tag{4.9}$$

where D_0 is the diffusion coefficient.

At the fluid–solid interface, the continuity of velocity and traction is enforced

$$\boldsymbol{v} = \frac{\partial \boldsymbol{u}}{\partial t}, \tag{4.10}$$

$$\boldsymbol{n}\cdot\boldsymbol{\sigma}_{\boldsymbol{s}} = \boldsymbol{n}\cdot\big[-p\boldsymbol{I} + \eta\big(\boldsymbol{\nabla}\boldsymbol{v} + (\boldsymbol{\nabla}\boldsymbol{v})^{T}\big)\big], \tag{4.11}$$

where $\boldsymbol{n}$ is a unit vector normal to the solid boundary. This equation enforces the continuity of traction across the fluid–solid interface, where $\boldsymbol{\sigma}_{\boldsymbol{s}} = \mathcal{J}^{-1}\boldsymbol{F}\boldsymbol{S}\boldsymbol{F}^{\boldsymbol{T}}$ is the Cauchy stress tensor in the solid domain, and the right-hand side represents the total fluid stress acting on the interface. This fully coupled system of fluid flow, solid deformation and fluid diffusion equations is solved numerically using the finite-element-based method in COMSOL Multiphysics environment.

The simulations were performed in two dimensions over the half-height of the channel, exploiting symmetry about the centreline, as illustrated in figure 3(*a*). Fluid enters the channel from the inlet at a prescribed constant flow rate and exits at the outlet at zero pressure. The swelling solid is bonded to a rigid, impermeable surface, where both displacement and fluid flux are set to zero. At the lateral boundaries of the solid domain ($x = 0$ and $x = l$), roller constraints are imposed to enforce a zero-displacement condition in the longitudinal direction $u_x = 0$. This ensures that the solid edges remain fixed axially, while permitting unconstrained deformation in the transverse direction (y-direction) due to swelling and fluid pressure.

It should be noted that the roller boundary condition ensures that the solid is free to deform only along the y-direction at the inlet. However, this boundary condition is a significant simplification of real-world experimental systems, such as those reported by Gervais *et al.* (2006), Hardy *et al.* (2009) and Raj M *et al.* (2018). Consequently, the present analysis is valid outside the boundary layers, far from the injection points (Christov

https://doi.org/10.1017/jfm.2026.11866 Published online by Cambridge University Press

Parameters	Symbol	Values
Length	l	1–10 cm
Channel's half-height	h_{0f}	50–500 μm
Solid's thickness	h_{0s}	0.1–10 mm
Flow rate per unit width	q	10^{-8}–10^{-6} m^2/s
Fluid viscosity	η	10^{-3} Pa.s
Young's modulus	E	10–10^3 kPa
Poisson's ratio	ν	0.3–0.5
Swelling ratio	$\Delta_{s,\infty}/h_{0s}$	10^{-1}
Flow time scale	t_f	1–10^3 s
Diffusion coefficient	D	10^{-11}–10^{-9} m^2/s
Swelling time scale	t_s	10^2–10^4 s
Absorption ratio	α	0.5–1.5

Table 1. Physical parameters.

et al. 2018). In experimental realisations of flow through soft channels, deformations in boundary layers lead to intriguing fluid–structure interaction (FSI) phenomena, such as choking, which are discussed by Box *et al.* (2020) and Peng *et al.* (2023).

4.2. *Numerical method*

The fully coupled fluid–structure diffusion problem is solved using COMSOL Multiphysics, which employs the finite element method to simulate multiphysics interactions. The governing equations for fluid flow, solid deformation and fluid diffusion, given by equations (4.1), (4.2), (4.3) and (4.9), were cast into their weak forms and discretised over the computational domain. Both the fluid and solid domains are discretised using triangular finite elements. To accurately resolve gradients near the fluid–solid interface, locally refined, structured elements are employed in this region. Mesh motion arising from solid deformation is handled using COMSOL's built-in arbitrary Lagrangian–Eulerian formulation. The governing equations are integrated in time using a variable-step backward differential formula method with relative tolerance of 10^{-3}. Within each time step, nonlinearities are handled via the Newton method. The resulting linearised sub-problems are solved using the parallel direct sparse solver direct solver, which ensures that the linear residuals are reduced to the limit of machine precision. The mesh-independence test results are provided in Appendix A. The final mesh utilised ensured that the numerical results are independent of the spatial discretisation.

5. Results and discussion

The coupled evolution of the flow domain, driven by swelling-induced deformation of the bounding walls and fluid-pressure-mediated elastic response, gives rise to spatio-temporal variation of the flow rate and velocity field along the channel. The resulting dynamics depends sensitively on the mode of flow actuation, as well as on the mechanical and transport properties of both the fluid and the solid.

To demonstrate these effects under experimentally relevant conditions, we adopt material and flow parameters representative of microfluidic and biological systems, as summarised in table 1 (Hardy *et al.* 2009; Yoon *et al.* 2010; Cheung *et al.* 2012; Anez *et al.* 2021). Consistent with the weak-swelling assumption underlying the theoretical development, we limit our analysis to small swelling ratios, appropriate for microfluidic

https://doi.org/10.1017/jfm.2026.11866 Published online by Cambridge University Press

Parameters	Symbol	Values
Aspect ratio	$\epsilon = h_{0f}/l$	$\sim 10^{-2}$
Solid aspect ratio	$\epsilon_s = h_{0s}/l$	10^{-2}–10^{-1}
Solid to channel height ratio	$r = h_{0s}/h_{0f}$	1–10
Collapse ratio	$\beta = \Delta_{s,\infty}/h_{0f}$	0.1–1
Modified Reynolds number	$Re = \epsilon Re^*$	10^{-4}–10^{-2}
Strouhal number	St	10^{-2}–1
Fluid-pressure scale	p_0	10^{-2}–1
Compliance parameter	ϱ	10^{-4}–10^{-6}

Table 2. Ranges of non-dimensional parameters.

applications. We emphasise that this choice reflects a modelling assumption rather than a limitation of swelling phenomena, as many polymeric solids can exhibit swelling ratios far exceeding their initial volume ($\gg 1$).

Using these material properties, we obtain the corresponding ranges of the relevant non-dimensional parameters, presented in table 2. These ranges form the basis for the analysis presented in next sub-sections, allowing us to examine the competing roles of swelling-induced collapse and fluid-pressure-driven restraint in shaping the flow dynamics.

The competing roles of swelling-induced collapse and fluid-pressure-driven restraint are primarily governed by the dimensionless parameters summarised in table 2. In the following sections, we explore the transient flow evolution by varying the collapse ratio $\beta = 0.1-1$, which dictates the magnitude of reduction in channel height, and the compliance parameter $\varrho \sim 10^{-4}-10^{-6}$ which governs the solid's responsiveness to the fluid pressure. This parameter space allows us to delineate the transition from a swelling-dominated dynamics to that significantly modified by FSI.

5.1. *Mathematical model validation*

We first validate the mathematical model by comparison with the fully coupled direct numerical simulation performed using COMSOL Multiphysics, following the methodology described in § 4. In figure 3(*b*), we illustrate the evolution of half-height of the channel, scaled with its instantaneous inlet value, $\overline{H}(X, T) = H(X, T)/H(0, T)$, where the overbar denotes the normalisation with its corresponding value at the inlet $X = 0$. The predictions of the nonlinear diffusion model, given by (3.30), and its approximate analytical solution, (3.34), are compared against the fully coupled direct numerical simulation (DNS) results for $\varrho = 1.5 \times 10^{-5} (\ll 1)$. The excellent agreement observed over the entire channel length and at all times establishes the quantitative validity of the mathematical model and confirms the accuracy of the asymptotic solution.

At early times $T \lesssim 1$, figure 3(*b*) shows that $\overline{H}(X, T) \approx 1$, indicating an approximately homogeneous deformation along the channel length dominated by swelling. At later times, however, $\overline{H}(X, T)$ decreases monotonically with X, reflecting the emergence of spatially non-uniform deformation. This non-uniformity arises from the substantial increase in fluid pressure at the inlet as the channel height decreases upon swelling of the bounding solids, as shown in figure 4(*b*). The elevated inlet pressure induces an elastic deformation of the solid that opposes further swelling-induced collapse, while the outlet, maintained at zero pressure, continues to deform due to swelling. As a result, the channel remains relatively more open at the inlet than at the outlet, as shown in figure 3(*b*). The difference between

https://doi.org/10.1017/jfm.2026.11866 Published online by Cambridge University Press

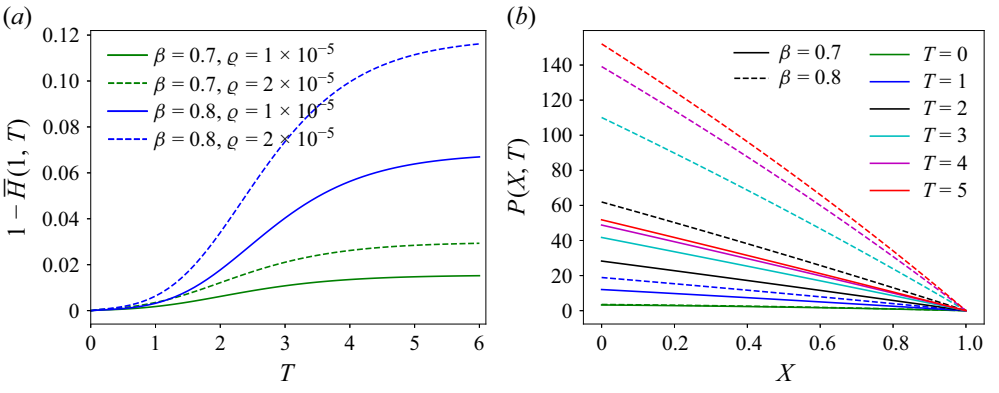


Figure 4. (*a*) Evolution of height disparity, defined as $1-\overline{H}(1,T)$ for different β and ϱ. (*b*) Evolution of fluid pressure $P(X,T)$ along the channel length for different collapse ratio β with compliance parameter $\varrho = 1.5\times10^{-5}$. For all cases, $\varkappa = 8$.

the inlet and outlet channel heights increases with time and reaches its maximum once swelling-induced deformation saturates ($T \gg 1$).

Before examining the transient evolution of the system, we define the asymptotic steady state ($T \to \infty$) toward which the channel evolves. In our model, the swelling kinetics saturate as the absorbed fluid concentration reaches equilibrium. For the characteristic time scales considered, the system effectively reaches a steady state by $T \approx 5$, where the swelling-induced deformation reaches its maximum value, as illustrated in figures 2 and 13. The flow field evolves from the initial condition at $T = 0$ to its steady state at $T = 5$.

5.2. *Effect of collapse ratio* (β) *and compliance parameter* (ϱ)

In figure 4(*a*), we illustrate the temporal evolution of the relative reduction in half-height of the channel at the outlet compared with the inlet, defined as $(H(0,T)-H(1,T))/H(0,T) = 1-\overline{H}(1,T)$, for different values of collapse ratio β and compliance parameters ϱ. For early times ($T \lesssim 1$), both the magnitude and slope of the relative reduction remain close to zero, indicating that spatial variations in deformation due to fluid pressure are negligible during the initial stages of swelling for the chosen values of β, ϱ and $\varkappa$. As swelling progresses, the reduction in channel height $H(X,T)$ leads to a substantial increase in fluid pressure, as shown in figure 4(*b*). The resulting pressure-induced deformation increasingly counteracts swelling near the inlet, while the outlet height remains unaffected by fluid-pressure-induced dilation. Consequently, the difference between the inlet and outlet channel height grows with time and eventually saturates once swelling-induced collapse ceases ($T \gg 1$, approximately $T \simeq 5$).

A larger collapse ratio β leads to a smaller gap height upon swelling, resulting in a significantly higher fluid pressure compared with cases with smaller β, as evident from figure 4(*b*). This enhanced fluid pressure more effectively restrains collapse near the inlet, thereby amplifying the difference between inlet and outlet channel heights, as shown in figure 4(*a*). In contrast, for small β, the pressure rise upon swelling is insufficient to generate a significant spatial variation in channel height. Similarly, increasing the compliance parameter ϱ enhances pressure-induced deformation of the solid, further promoting divergence between inlet and outlet heights. The resulting spatial asymmetry in the channel profile effectively determines the flow rectification of the system, as

https://doi.org/10.1017/jfm.2026.11866 Published online by Cambridge University Press

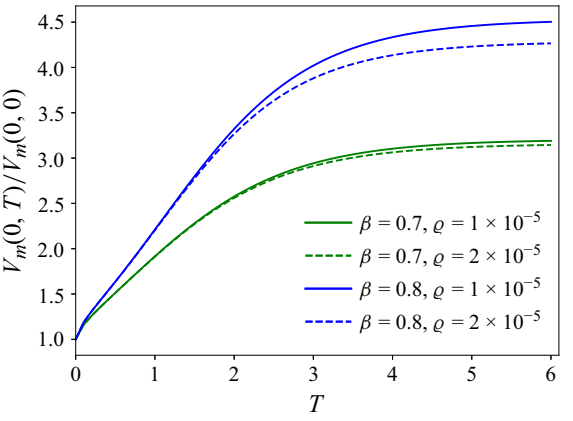


Figure 5. Evolution of the average inlet velocity $V_m(0, T)$ with time T, scaled with the corresponding value at $T = 0$, i.e. $V_m(0, 0)$, for different collapse ratios β and compliance parameters ϱ.

the hydrodynamic resistance becomes a dynamic function of the coupled swelling and pressure-induced deformations.

The dimensionless average fluid velocity is defined as $V_m(X, T) = Q(X, T)/2H(X, T)$. Since the inlet flow rate is fixed, $Q(0, T) = 1$, the average inlet velocity becomes $V_m(0, T) = 1/(2H(0, T))$. In figure 5, we illustrate the temporal evolution of the average inlet fluid velocity, scaled by its initial value $V_m(0, 0)$, for different values of β and ϱ. For a given compliance ϱ, a larger collapse ratio β leads to a smaller $H(0, T)$, and hence a higher inlet velocity. Conversely, for fixed β, increasing ϱ strengthens pressure-induced deformation, enlarges $H(0, T)$ and thereby reduces the inlet velocity.

The influence of absorption ratio α on $H(X, T)$, $P(X, T)$ and consequently on $V_m(0, T)$, is negligible in the present regime. This follows from (3.34), where the term containing α is proportional to $(\mathrm{d}A/\mathrm{d}T) \sim (1/t_s)$, rendering it orders of magnitude smaller than other dominant contributions, corresponding to $St \approx O(10^{-1})$. For rapid swelling ($t_s \sim 10^{-1}s$), which would require ultrathin solids ($\sim$1μm) and lead to $St \gg 1$, the effect of α could become significant, however, this regime lies outside the scope of the present study. Unlike the channel height and pressure, the absorption ratio α can significantly affect the flow rate and velocity distributions along the channel. For $\alpha > 1$, fluid absorption dominates over swelling, whereas for $\alpha < 1$, swelling exceeds absorption, governed by the mechano-chemical properties of the fluid–solid pair.

5.3. *High absorption ratio swelling* ($\alpha > 1$)

Certain soft solids absorb a large volume of fluid while exhibiting comparatively weak macroscopic swelling. This behaviour can arise from internal accommodation of the absorbed fluid, for instance through free volume (voids) or rearrangement of polymeric chains without significant expansion (Chang *et al.* 2020; Hoti *et al.* 2021). Without delving into the detailed chemical mechanisms governing α, we focus on elucidating its consequences on flow evolution within the channel.

The flow rate at any axial location $Q(X, T)$ can be obtained from (3.8) upon substituting the channel height $H(X, T)$ and $P(X, T)$. Using the relation $P(X, T) = (H(X, T) - A(T))/B(T)$ from (3.28), together with the expression of $H(X, T)$ from (3.34), we obtain the spatio-temporal variation of the flow rate as

$$Q(X, T) = 1 - 2(1 - \alpha)\frac{\mathrm{d}A}{\mathrm{d}T}X. \tag{5.1}$$

https://doi.org/10.1017/jfm.2026.11866 Published online by Cambridge University Press

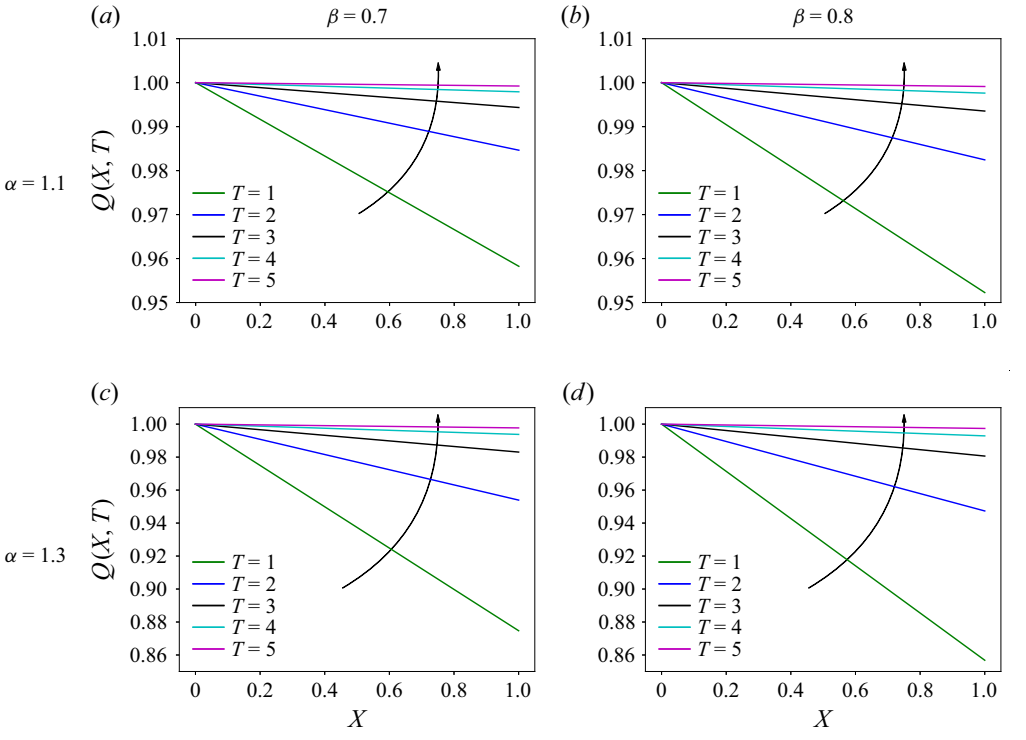


Figure 6. Evolution of the flow rate $Q(X, T)$ along the channel length for collapse ratios $\beta = 0.7$ and 0.8 and absorption ratios $\alpha = 1.1$ and 1.3, maintaining constant compliance parameter $\varrho = 1.5 \times 10^{-5}$ and $\varkappa = 8$.

In figure 6, we illustrate the evolution of the flow-rate variation $Q(X, T)$ along the channel length for different collapse ratios β and absorption ratios α. For solids with a high absorption ratio ($\alpha > 1$), the flow rate decreases linearly along the axial direction. At fixed β, increasing α leads to larger reduction in $Q(X, T)$, reflecting enhanced fluid absorption for the same degree of swelling. For a given absorption ratio, a larger collapse ratio β corresponds to a large swelling amplitude, resulting in increased absorption and hence stronger decay of flow rate along X. As time progresses and the swelling rate diminishes, fluid absorption weakens, and the flow rate becomes spatially uniform $Q(X, T) \to 1$, as illustrated in figure 6 for all α and β values.

The corresponding cross-sectionally averaged velocity can be obtained as $V_m(X, T) = Q(X, T)/2H(X, T)$, yielding

$$V_m(X, T) = \frac{1}{2H(X, T)}\left[1 - 2(1 - \alpha)\frac{\mathrm{d}A}{\mathrm{d}T}X\right]. \tag{5.2}$$

In figure 7, we illustrate the evolution of the cross-sectionally averaged velocity, scaled with its instantaneous value at the inlet, $\overline{V}_m(X, T) = V_m(X, T)/V_m(0, T)$ for different β and α values. This scaling isolates the effect of swelling–absorption and pressure-induced deformation on the spatio-temporal flow evolution along the channel length. The evolution of the inlet velocity $V_m(0, T)$ has been shown earlier in figure 5. At early times, $V_m(X, T)$ decreases linearly along X, mirroring the axial reduction in $Q(X, T)$, while spatial variations in $H(X, T)$ remain weak, as shown previously in figures 3 and 4. With increase in the values of β and α, the reduction in $\overline{V}_m(X, T)$ becomes significant. At later

https://doi.org/10.1017/jfm.2026.11866 Published online by Cambridge University Press

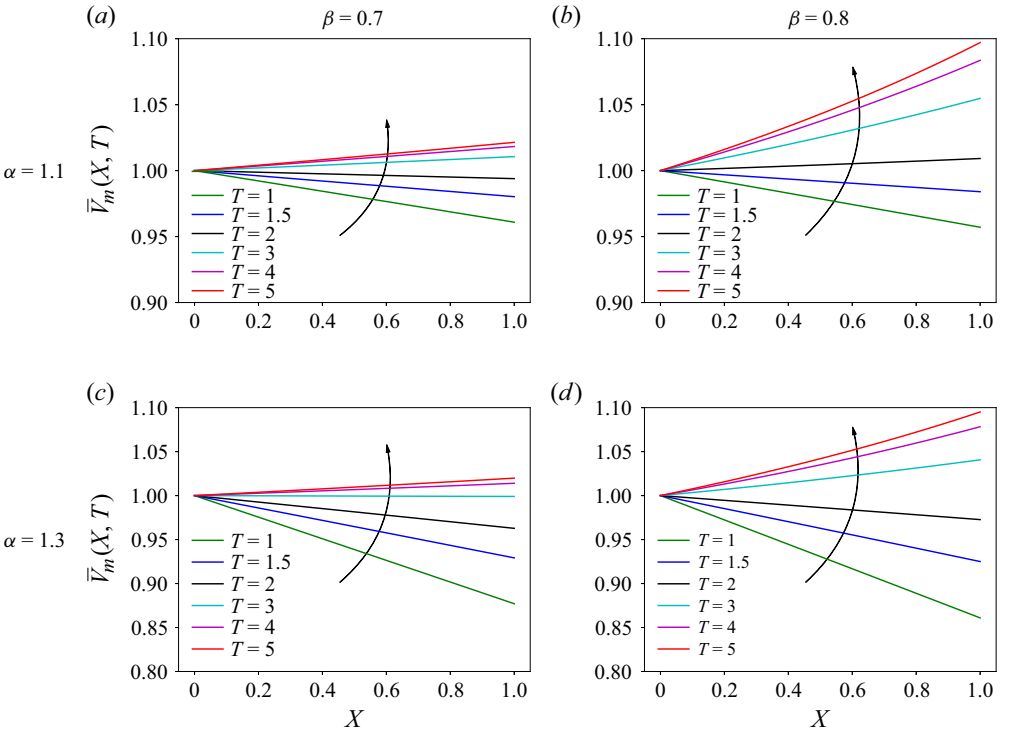


Figure 7. Evolution of cross-sectionally averaged flow velocity along the channel length, scaled by its instantaneous value at the inlet, $\overline{V}_m(X, T) = V_m(X, T)/V_m(0, T)$ for $\beta = 0.7$ and 0.8 and $\alpha = 1.1$ and 1.3, maintaining constant compliance parameter $\varrho = 1.5 \times 10^{-5}$ and $\varkappa = 8$.

times, as swelling subsides and the flow rate becomes nearly uniform along channel length, $Q(X, T) \approx 1$, as shown in figure 6, while spatial variations in $H(X, T)$ may become significant, depending on the collapse ratio β, shown earlier in figure 4. The decrease in $H(X, T)$ along X, while $Q(X, T) \approx 1$, leads to an increase in $V_m(X, T)$, causing the scaled velocity $\overline{V}_m(X, T)$ to exceed 1 along the channel length.

While the velocity profiles $\overline{V}_m(X, T)$ at early times appear approximately linear, a distinct nonlinear upward curvature emerges in the steady-state profiles ($T = 5$) for cases with high collapse ratios and compliance (figures 7*b* and 7*d*). This nonlinearity is a direct consequence of the non-uniform channel deformation; the high fluid pressure at the inlet partially restrains swelling-induced collapse, whereas the decreasing pressure towards the outlet allows for maximum collapse. To maintain a constant volumetric flow rate at steady state, the flow must accelerate, as evidenced by the concave-upward nonlinear curvature of the profile corresponding to $T = 5$. This transition marks the cross-over from a swelling–absorption-dominated regime to one governed primarily by fluid-pressure-induced deformation. Importantly, this pressure-driven flow distribution is itself strengthened by swelling-induced collapse and is critically controlled by the collapse ratio β for fixed values of ϱ and $\varkappa$.

5.4. *Low absorption ratio swelling* ($\alpha < 1$)

In contrast to the high-absorption scenario, certain soft solids absorb a relatively small volume of fluid while exhibiting pronounced swelling. This behaviour may arise

https://doi.org/10.1017/jfm.2026.11866 Published online by Cambridge University Press

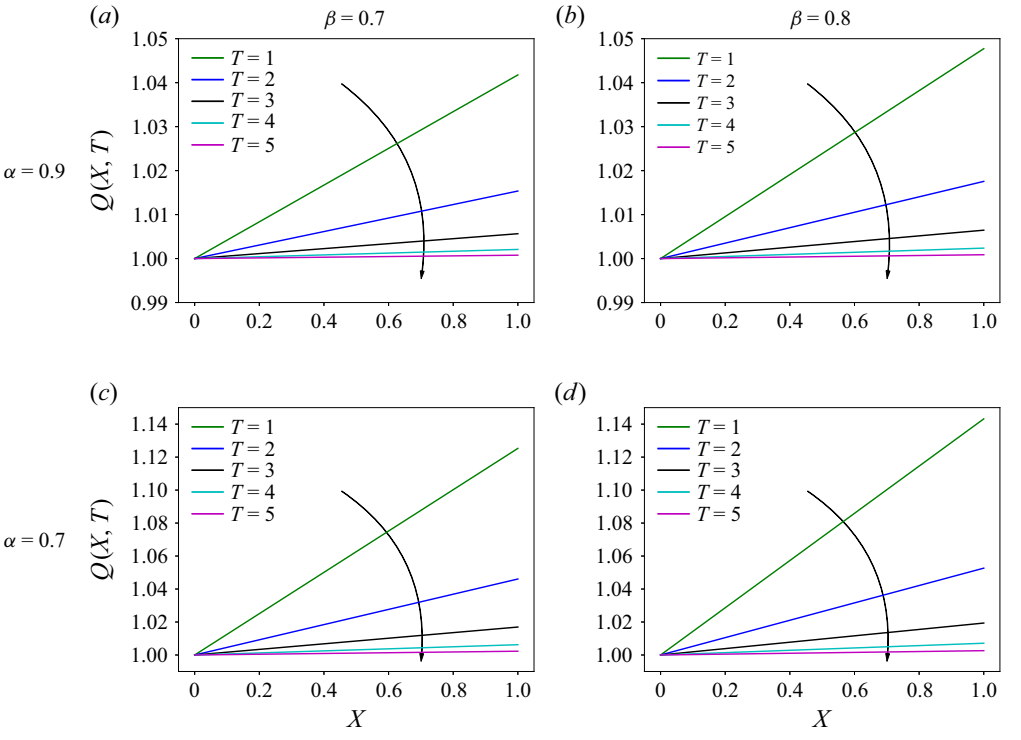


Figure 8. Evolution of the flow rate $Q(X, T)$ along the channel length for collapse ratios $\beta = 0.7$ and 0.8 and absorption ratios $\alpha = 0.7$ and 0.9, maintaining constant compliance parameter $\varrho = 1.5 \times 10^{-5}$ and $\varkappa = 8$.

from network loosening induced by fluid–polymer interaction, leading to significant macroscopic expansion despite limited uptake of fluid (Masoodi *et al.* 2010; Hoti *et al.* 2021). Under flow-rate-controlled inlet conditions, this property leads to an increase in flow rate along the channel, driven primarily by the collapsing motion of the bounding solid which dominating over fluid absorption.

In figure 8, we illustrate the evolution of axial flow rate $Q(X, T)$ for different values of the collapse ratio β and absorption ratio $\alpha < 1$. In this scenario, the flow rate increases linearly along the channel length because the rate of fluid displacement by the encroaching walls exceeds the rate of fluid absorbed into the walls. This transient effect is governed by the absorption ratio α. For $\alpha < 1$, the contraction of the fluid domain due to swelling of solid wall acts as a net source for the volumetric flux. For fixed β, lower values of α (i.e. farther from 1) lead to a steeper axial increase in $Q(X, T)$. Similarly, a larger collapse ratio β corresponds to enhanced swelling, resulting in greater wall displacement and hence a larger rise in flow rate along X. As the swelling rate decays with time, the flow rate gradually becomes spatially uniform $Q(X, T) \to 1$, as observed in figure 8.

In figure 9, we illustrate the evolution of scaled average velocity $\overline{V}_m(X, T)$ for the low-absorption scenario, $\alpha < 1$. At early times, $V_m(X, T)$ increases linearly with X, following the axial rise in $Q(X, T)$, while spatial variation in $H(X, T)$ remains insignificant, which is pronounced for larger β and smaller α values. As swelling subsides and the flow rate becomes nearly uniform along the channel length $Q(X, T) \approx 1$, the axial gradient $\partial \overline{V}_m / \partial X$ reduces. However, at later times, an interesting transition can be observed, once spatial variations in the channel height become significant, i.e. $1 - \overline{H}(X, T)$ grows

https://doi.org/10.1017/jfm.2026.11866 Published online by Cambridge University Press

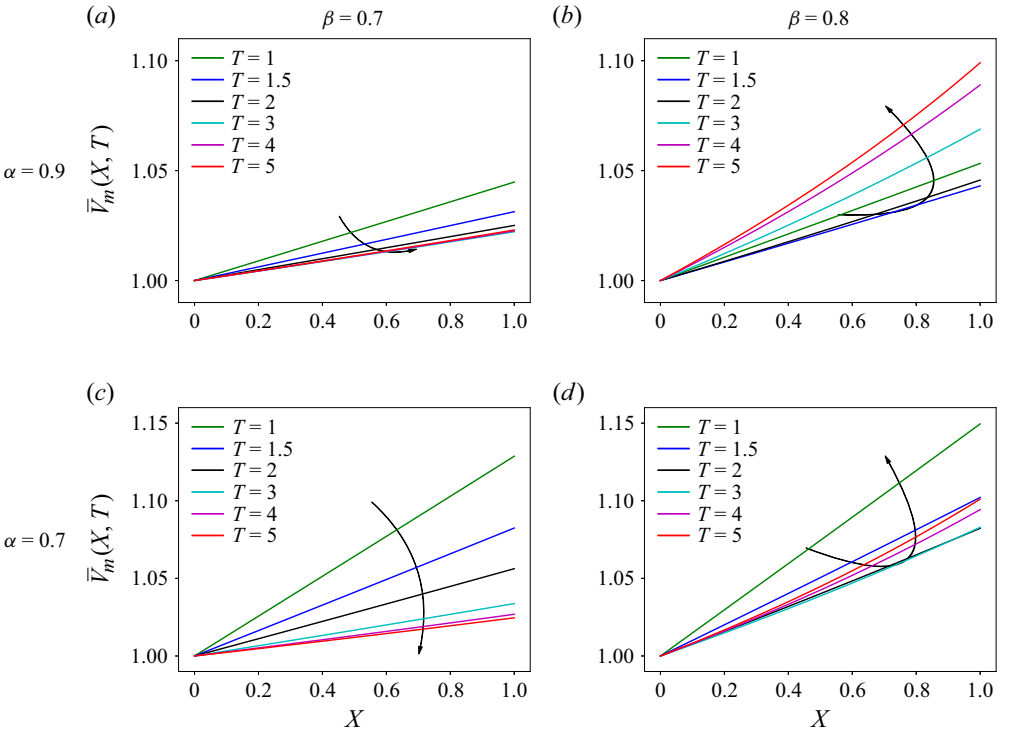


Figure 9. Evolution of the cross-sectionally averaged flow velocity along the channel length, scaled by its instantaneous value at the inlet $\overline{V}_m(X, T) = V_m(X, T)/V_m(0, T)$ for $\beta = 0.7$ and 0.8 and $\alpha = 0.7$ and 0.9, maintaining constant compliance parameter $\varrho = 1.5 \times 10^{-5}$ and $\varkappa = 8$.

appreciably. This eventually leads to a rise in $\overline{V}_m(X, T)$ again, after slight flattening upon reduction in swelling rate, as shown in figure 9. Therefore, the velocity evolution is non-monotonic: an initial linear increase driven by swelling-dominated wall motion, followed by weakening of axial variation as swelling decays and ultimately a nonlinear increase governed by fluid-pressure-induced deformation. This transition is controlled jointly by the collapse ratio β, compliance parameter ϱ and $\varkappa$.

5.5. *Regime of transition: swelling to fluid-pressure dominated*

In figures 7 and 9, we demonstrated that the flow velocity can transition from a swelling-dominated linear decrease or increase to a nonlinear increase driven by fluid pressure, as the channel collapses due to swelling. However, such a transition is not guaranteed, and depends critically on the governing dimensionless parameters- β, ϱ and $\varkappa$, whose values were carefully chosen in earlier sub-sections to illustrate this evolution. For sufficiently small collapse ratio β or very small compliance parameter ϱ, fluid pressure may remain insignificant at all times. Conversely, for sufficiently large compliance, the fluid pressure may significantly deform the channel from the outset ($T = 0$). As a result, the flow evolution can exhibit qualitatively different behaviours depending on the values of β, ϱ and $\varkappa$.

In general, the flow evolution can be categorised into three distinct regimes: (i) a swelling-dominated regime, in which fluid-pressure-induced deformation remains negligible throughout the evolution, (ii) a transitional regime, in which the flow evolves

https://doi.org/10.1017/jfm.2026.11866 Published online by Cambridge University Press

from swelling-dominated behaviour at early times to fluid-pressure-dominated behaviour at later times, and (iii) a pressure-dominated regime, in which fluid-pressure-induced deformation is significant from the onset of swelling. The transitional regime lies between the two limiting cases corresponding to regimes (i) and (iii), which we now delineate.

Case I: swelling-dominated regime. In this regime, swelling alone governs the evolution of channel geometry and flow velocity, while the effect of fluid pressure remains negligible at all times. Consequently, the channel height remains nearly uniform along the flow direction. To quantify this, we require the relative difference between the inlet and outlet half-heights to remain below a prescribed threshold δ, i.e. $1-\overline{H}(1,T)\leq\delta$, ensuring that pressure-induced deformation can be neglected. As swelling progresses, the channel height decreases and the fluid pressure increases, attaining its maximum value upon cessation of swelling at $T\to\infty$. Using the analytical expression for $H(X,T)$ from (3.34), with $\mathcal{F}_n=1$ and $\mathrm{d}A/\mathrm{d}T=0$ as $T\to\infty$, yields the condition

$$\frac{\varrho\,(\beta+\varkappa)}{(1-\beta)^4}\leq\frac{2\delta}{3}, \tag{5.3}$$

which defines the swelling-dominated regime, corresponding to the region lying below the surface defined by the equality in (5.3).

Case III: pressure-dominated regime. In this regime, the fluid-pressure-induced deformation is significant from the onset $T=0$. Accordingly, the relative difference in channel half-height between the inlet and outlet exceeds the threshold δ at $T=0$, i.e. $1-\overline{H}(1,T=0)\geq\delta$. Using $\mathcal{F}_n(T=0)=0$, and $\mathrm{d}A/\mathrm{d}T=-\beta\mathcal{F}_n'(T=0)$, yields the criterion

$$\varrho\varkappa\left[1+(1-\alpha)\beta\mathcal{F}_n'(0)\right]\geq\frac{2\delta}{3}. \tag{5.4}$$

This regime lies above the surface defined by equality in (5.4).

The regime diagram in figure 10 illustrates the three distinct behaviours in the (ϱ,β,∇) parameter space. The blue surface corresponds to (5.3) and separates the swelling-dominated regime below it, for which fluid pressure never significantly influences the channel geometry or flow. The green surface corresponds to (5.4) and demarcates the pressure-dominated regime above it, in which the fluid pressure remains important throughout the evolution. The region enclosed between these two surfaces gives rise to the transitional regime, characterised by an evolution from swelling-dominated flow at early times to fluid-pressure-dominated flow at later times, as demonstrated in figures 7 and 9. Notably, as β decreases, the transitional region narrows significantly, confirming that the coupling between swelling and fluid pressure is less pronounced for smaller collapse ratios. The representative cases discussed in §§ 5.3 and 5.4 ($\beta=0.7$ and $\beta=0.8$) lie within this transitional envelope, serving as archetypes for the non-monotonic flow behaviour observed across the broader parametric range.

6. Summary and conclusion

In this paper, we have investigated the flow dynamics in a shallow rectangular microchannel bounded by compliant walls that can swell upon fluid absorption, under inlet flow-rate-controlled conditions. The solid deformation is modelled using a linear - elastic, linear swelling framework, with the assumption of weak swelling ($\beta/\varkappa\ll1$), such that deformations induced by swelling and fluid pressure remain small compared with the solid thickness and variations in material properties can be neglected. Within this regime, we developed an unsteady lubrication-based mathematical framework that captures the

https://doi.org/10.1017/jfm.2026.11866 Published online by Cambridge University Press

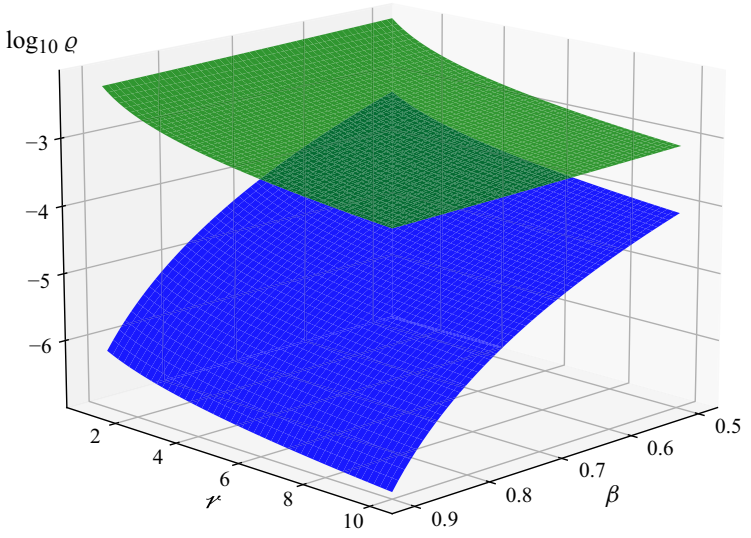


Figure 10. Three-dimensional plot illustrating the two surfaces which separate the entire $\varrho - \beta - \varkappa$ parameter space into three regimes using $\delta = 2\,\%$. The different regimes are: (*i*) swelling-dominated regime, lying below the blue surface, (ii) transitional regime, which is sandwiched between the blue and green surfaces, and (iii) pressure-dominated regime, which lies above the green surface.

coupled evolution of the flow field and channel geometry arising from both swelling and fluid-pressure-induced deformations. The analysis leads to a nonlinear diffusion equation governing the spatio-temporal evolution of the channel height, for which a simple analytical solution was obtained in the limit of small compliance parameter $\varrho \ll 1$.

The validity of the mathematical model and its analytical solution was assessed through fully coupled two-dimensional direct numerical simulations, and excellent agreement was found between them. The results demonstrate that swelling-induced channel collapse leads to a substantial rise in fluid pressure, which progressively counteracts further collapse. The combined effects of swelling and fluid pressure significantly enhance the inlet velocity under constant flow-rate actuation.

We further showed that swelling-driven collapse can fundamentally alter the flow distribution along the channel. Depending on the absorption ratio α, collapse ratio β, compliance parameter ϱ and $\varkappa$, the flow may remain swelling dominated, become fluid-pressure dominated from the outset or undergo a transition from swelling-dominated behaviour at early times to fluid-pressure-dominated behaviour at later times. These distinct flow evolutions were systematically classified by delineating regimes in the $(\varrho, \beta, \varkappa)$ parameter space and determining the range of values of these parameters that trigger these distinct flow behaviours.

Beyond these specific physical insights, the present work establishes a general framework for analysing transport through swelling-compliant microchannels. The principles elucidated here are broadly applicable to systems in which fluid flow, solid deformation and mass transport are strongly coupled, and may inform strategies for controlling flow and transport by tuning swelling behaviour through material choice or external actuation. Furthermore, the coupling between wall compliance and non-uniform swelling provides a mechanism for flow rectification, suggesting that these responsive microchannels can serve as a theoretical basis for designing self-regulating fluidic diodes. By integrating soft-matter mechanics, hydrodynamics and fluid absorption into a unified

https://doi.org/10.1017/jfm.2026.11866 Published online by Cambridge University Press

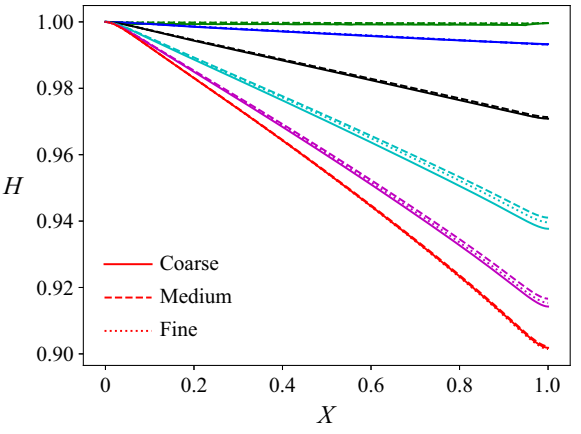


Figure 11. Comparison of $\overline{H}$ vs X at different times T for coarse, medium and fine meshes, demonstrating mesh independence. Colour coding of lines: green: $T = 0$, blue: $T = 1$, black: $T = 2$, cyan: $T = 3$, magenta: $T = 4$, red: $T = 5$.

description, this study provides a foundation for the design of responsive microfluidic and bio-inspired flow-control systems.

Acknowledgements. K.K. acknowledges the Ministry of Education, Govt. of India, for the Prime Minister's Research Fellowship. S.C. acknowledges SERB, Department of Science and Technology, Government of India, for the Sir J.C. Bose National Fellowship.

Declaration of interests. The authors declare no conflict of interest.

Appendix A. Mesh-independence test

To ensure convergence of our FSI simulations, we performed a mesh-independence test using three levels of refinement: coarse (27 804 elements), medium (74 364 elements) and fine (98 866 elements). The grid convergence threshold was defined by a relative change in $\overline{H}$ of less than 0.5 % at the outlet $X = 1$. As shown in figure 11 (Appendix A), the spatial distribution of the channel height $\overline{H}$ remains consistent across the medium and fine meshes, demonstrating that the simulation results are independent of the mesh. The medium mesh was utilised for all results to optimise computational efficiency without sacrificing accuracy.

Appendix B. Further validation of the mathematical model

To further validate the robustness of our theoretical framework, we compare the spatio-temporal evolution of the channel height predicted by (3.34) with direct numerical simulations performed in COMSOL. As shown in figure 12, the model shows excellent agreement with DNS across varying compliance parameter ϱ, swelling ratio β and solid to fluid height ratio $\varkappa$.

Appendix C. Evolution of channel height

We present the spatial variation of the absolute channel height $H(X, T)$ at different times T, to illustrate the global collapse of the fluid domain due to swelling. While figure 13 captures the significant reduction in channel height H due to swelling, the spatial gradients along the channel length X are obscured by the vertical scale. Consequently, we utilised

https://doi.org/10.1017/jfm.2026.11866 Published online by Cambridge University Press

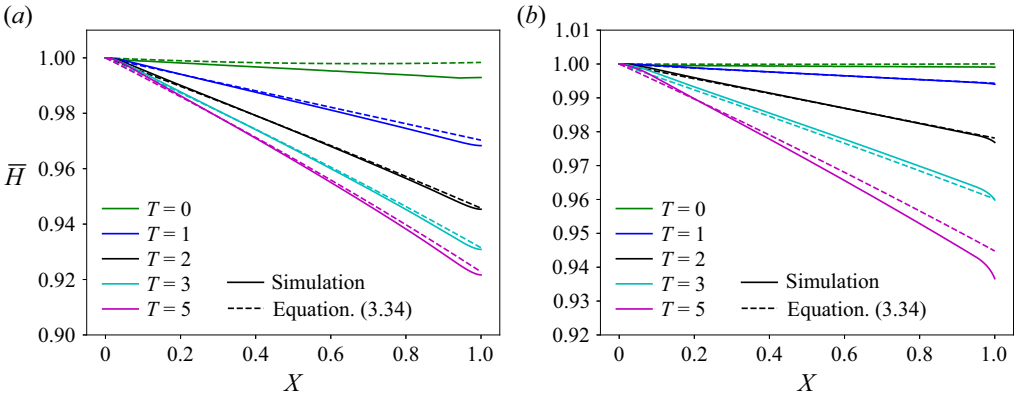


Figure 12. Comparison of $\overline{H}$ vs X for various times T for parameters: (*a*) $\beta = 0.5$, $\varkappa = 8$, $\varrho = 4.7 \times 10^{-4}$, and (*b*) $\beta = 0.75$, $\varkappa = 6$, $\varrho = 3.5 \times 10^{-5}$.

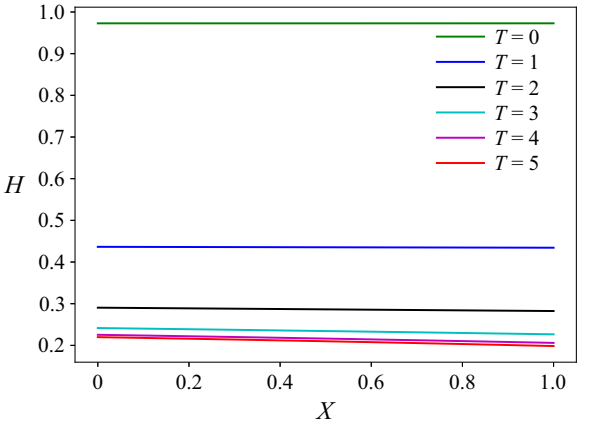


Figure 13. Comparison of $H(X, T)$ vs X at different times T for $\beta = 0.8$, $\varkappa = 8$, $\varrho = 1.5 \times 10^{-5}$.

the normalised height $\overline{H}(X, T) = H(X, T)/H(0, T)$ to isolate and analyse the pressure-driven deformation mechanisms.

References

Anand, V. & Christov, I.C. 2021 Revisiting steady viscous flow of a generalized Newtonian fluid through a slender elastic tube using shell theory. *Z. Angew. Math. Mech.* **101** (2), e201900309.

Anez, V., Hadji, D., Santanach-Carreras, C., Lorenceau, E., Picard, E. & C 2021 Microfluidic channels of adjustable height using deformable elastomer. *Microfluid Nanofluid* **25** (1), 7.

Bhattacharyya, K., Zwicker, D. & Alim, K. 2023 Memory capacity of adaptive flow networks. *Phys. Rev. E* **107** (3), 034407.

Bouklas, N. & Huang, R. 2012 Swelling kinetics of polymer gels: comparison of linear and nonlinear theories. *Soft Matt.* **8** (31), 8194–8203.

Box, F., Peng, G.G., Pihler-Puzović, D. & Juel, A. 2020 Flow-induced choking of a compliant Hele-Shaw cell. *Proc. Acad. Nat. Sci. USA* **117** (48), 30228–30233.

Bruus, H. 2011 *Theoretical Microfluidics*, Reprinted with corr. Oxford University Press.

Chakraborty, S. 2010 *Microfluidics and Microfabrication*. Springer US.

Chang, S., Jensen, K.H., Kim, H.-Y. & Kim, W. 2022 Dynamics of water imbibition through hydrogel-coated capillary tubes. *Phys. Rev. Fluids* **7** (6), 064301.

https://doi.org/10.1017/jfm.2026.11866 Published online by Cambridge University Press

CHANG, S., KIM, H.-Y. & KIM, W. 2020 Dynamics of water imbibition through paper with swelling. *J. Fluid Mech.* **892**, A39.

CHEN, S., HUANG, R. & RAVI-CHANDAR, K. 2020 Linear and nonlinear poroelastic analysis of swelling and drying behavior of gelatin-based hydrogels. *Intl J. Solids Struct.* **195**, 43–56.

CHEUNG, P., TODA-PETERS, K. & SHEN, A.Q. 2012 *In situ* pressure measurement within deformable rectangular polydimethylsiloxane microfluidic devices. *Biomicrofluidics* **6** (2), 026501.

CHRISTOV, I.C. 2022 Soft hydraulics: from Newtonian to complex fluid flows through compliant conduits. *J. Phys.: Condens. Matter* **34** (6), 063001.

CHRISTOV, I.C., COGNET, V., SHIDHORE, T.C. & STONE, H.A. 2018 Flow rate–pressure drop relation for deformable shallow microfluidic channels. *J. Fluid Mech.* **841**, 267–286.

DANGLA, R., GALLAIRE, F. & BAROUD, C.N. 2010 Microchannel deformations due to solvent-induced PDMS swelling. *Lab Chip* **10** (21), 2972–2978.

DROZDOV, A.D., SOMMER-LARSEN, P., DE CLAVILLE CHRISTIANSEN, J. & SANPOREAN, C.-G. 2014 Time-dependent response of hydrogels under constrained swelling. *J. Appl. Phys.* **115** (23), 233517.

DUPRAT, C. 2022 Moisture in textiles. *Annu. Rev. Fluid Mech.* **54** (1), 443–467.

DUPRAT, C. & STONE, H.A. (Eds) 2015 *Fluid–Structure Interactions in Low-Reynolds-Number Flows*, pp. 280–312. The Royal Society of Chemistry.

ELBAZ, S.B. & GAT, A.D. 2014 Dynamics of viscous liquid within a closed elastic cylinder subject to external forces with application to soft robotics. *J. Fluid Mech.* **758**, 221–237.

ELBAZ, S.B. & GAT, A.D. 2016 Axial creeping flow in the gap between a rigid cylinder and a concentric elastic tube. *J. Fluid Mech.* **806**, 580–602.

GERVAIS, T., EL-ALI, J., GÜNTHER, A. & JENSEN, K.F. 2006 Flow-induced deformation of shallow microfluidic channels. *Lab on a Chip* **6** (4), 500.

GONZÁLEZ-ESTEFAN, J.H., GONIDEC, M., VU, T.T., DARO, N. & CHASTANET, G. 2019 In situ fine-tuning of microfluidic chips by swelling and its application to droplet microfluidics. *Adv. Mater. Technol.* **4** (8), 1900232.

HARDY, B.S., UECHI, K., ZHEN, J. & PIROUZ KAVEHPOUR, H. 2009 The deformation of flexible PDMS microchannels under a pressure driven flow. *Lab on a Chip* **9** (7), 935–938.

HEIL, M. & HAZEL, A.L. 2011 Fluid-structure interaction in internal physiological flows. *Annu. Rev. Fluid Mech.* **43** (1), 141–162.

HOTI, G., CALDERA, F., CECONE, C., RUBIN PEDRAZZO, A., ANCESCHI, A., APPLETON, S.L., KHAZAEI MONFARED, Y. & TROTTA, F. 2021 Effect of the cross-linking density on the swelling and rheological behavior of ester-bridged β-cyclodextrin nanosponges. *Materials* **14** (3), 478.

INAMDAR, T.C., WANG, X. & CHRISTOV, I.C. 2020 Unsteady fluid-structure interactions in a soft-walled microchannel: a one-dimensional lubrication model for finite Reynolds number. *Phys. Rev. Fluids* **5** (6), 064101.

KARAN, P., CHAKRABORTY, J., CHAKRABORTY, S., WERELEY, S.T. & CHRISTOV, I.C. 2021 Profiling a soft solid layer to passively control the conduit shape in a compliant microchannel during flow. *Phys. Rev. E* **104** (1), 015108.

KAWARA, S., CUNNINGHAM, B., BEZER, J., KC, N., ZHU, J., TANG, M.X., ISHIHARA, J., CHOI, J.J. & AU, S.H. 2023 Capillary-scale hydrogel microchannel networks by wire templating. *Small* **19** (42), 2301163.

KESHMIRI, K., HUANG, H. & NAZEMIFARD, N. 2019 Compatibility of poly(dimethylsiloxane) microfluidic systems with high viscosity hydrocarbons. *SN Appl. Sci.* **1** (7), 1–11.

KIM, M.M., HUANG, Y., CHOI, K. & HIDROVO, C.H. 2014 The improved resistance of PDMS to pressure-induced deformation and chemical solvent swelling for microfluidic devices. *Microelectron. Engng* **124**, 66–75.

KNOBLAUCH, J., DROBNITCH, S.T., PETERS, W.S. & KNOBLAUCH, M. 2016 In situ microscopy reveals reversible cell wall swelling in kelp sieve tubes: one mechanism for turgor generation and flow control? *Plant Cell Environ.* **39** (8), 1727–1736.

KOLDAEVA, A., TSAI, H., SHEN, A.Q. & PIGOLOTTI, S. 2022 Population genetics in microchannels. *Proc. Natl Acad. Sci. USA* **119** (12), e2120821119.

KRAMER, F. & MODES, C.D. 2023 Biological flow networks: antagonism between hydrodynamic and metabolic stimuli as driver of topological transitions. *Phys. Rev. Res.* **5** (2), 023106.

KVICK, M., MARTINEZ, D.M., HEWITT, D.R. & BALMFORTH, N.J. 2017 Imbibition with swelling: capillary rise in thin deformable porous media. *Phys. Rev. Fluids* **2** (7), 074001.

LI, Y. & TANAKA, T. 1990 Kinetics of swelling and shrinking of gels. *J. Chem. Phys.* **92** (2), 1365–1371.

LIU, Q., ROBISSON, A., LOU, Y. & SUO, Z. 2013 Kinetics of swelling under constraint. *J. Appl. Phys.* **114** (6), 064901.

https://doi.org/10.1017/jfm.2026.11866 Published online by Cambridge University Press

LOUF, J.-F., KNOBLAUCH, J. & JENSEN, K.H. 2020 Bending and stretching of soft pores enable passive control of fluid flows. *Phys. Rev. Lett.* **125** (9), 098101.

M, K.R., DASGUPTA, S. & CHAKRABORTY, S. 2019 Biomimetic pulsatile flows through flexible microfluidic conduits. *Biomicrofluidics* **13** (1), 014103.

MARTÍNEZ-CALVO, A., SEVILLA, A., PENG, G.G. & STONE, H.A. 2020 Start-up flow in shallow deformable microchannels. *J. Fluid Mech.* **885**, A25.

MASOODI, H.R., MASOODI, R. & PILLAI, K.M. 2010 Darcy's law-based model for wicking in paper-like swelling porous media. *AIChE J.* **56** (9), 2257–2267.

MEHBOUDI, A. & YEOM, J. 2019 Experimental and theoretical investigation of a low-Reynolds-number flow through deformable shallow microchannels with ultra-low height-to-width aspect ratios. *Microfluid Nanofluid* **23** (5), 66.

MEIGEL, F.J. & ALIM, K. 2018 Flow rate of transport network controls uniform metabolite supply to tissue. *J. R. Soc. Interface* **15** (142), 20180075.

PANDA, P., YUET, K.P., DENDUKURI, D., ALAN HATTON, T. & DOYLE, P.S. 2009 Temporal response of an initially deflected PDMS channel. *New J. Phys.* **11** (11), 115001.

PARK, K., TIXIER, A., PALUDAN, M., ØSTERGAARD, E., ZWIENIECKI, M. & JENSEN, K.H. 2021 Fluid-structure interactions enable passive flow control in real and biomimetic plants. *Phys. Rev. Fluids* **6** (12), 123102.

PATARI, S., CHOWDHURY, I.U., KUMAR, J. & MAHAPATRA, P.S. 2023 Dynamics of liquid flow through fabric porous media: experimental, analytical, and numerical investigation. *Phys. Fluids* **35**, 103305.

PENG, G.G., CUTTLE, C., MACMINN, C.W. & PIHLER-PUZOVIĆ, D. 2023 Axisymmetric gas–liquid displacement flow under a confined elastic slab. *Phys. Rev. Fluids* **8** (9), 094005.

POLYGERINOS, P., CORRELL, N., MORIN, S.A., MOSADEGH, B., ONAL, C.D., PETERSEN, K., CIANCHETTI, M., TOLLEY, M.T. & SHEPHERD, R.F. 2017 Soft robotics: review of fluid-driven intrinsically soft devices; manufacturing, sensing, control, and applications in Human–Robot interaction. *Adv. Engng Mater.* **19** (12), 1700016.

RAJ, A., HALDER, R., SAJEESH, P. & SEN, A.K. 2016 Droplet generation in a microchannel with a controllable deformable wall. *Microfluid Nanofluid* **20** (7), 102.

RAJ, A. & SEN, A.K. 2016 Flow-induced deformation of compliant microchannels and its effect on pressure–flow characteristics. *Microfluid Nanofluid* **20** (2), 31.

RAJ, A., SUTHANTHIRARAJ, P.P.A. & SEN, A.K. 2018 Pressure-driven flow through PDMS-based flexible microchannels and their applications in microfluidics. *Microfluid Nanofluid* **22** (11), 128.

RAJ, M., PRIYADARSHANI, K., KARAN, J., BANDYOPADHYAY, P., BHATTACHARYA, S., CHAKRABORTY, S. & S 2023 Bio-inspired microfluidics: a review. *Biomicrofluidics* **17** (5), 051503.

RAJ, M.K., CHAKRABORTY, J., DASGUPTA, S. & CHAKRABORTY, S. 2018 Flow-induced deformation in a microchannel with a non-Newtonian fluid. *Biomicrofluidics* **12** (3), 034116.

RAJ, M.K., DASGUPTA, S. & CHAKRABORTY, S. 2017 Hydrodynamics in deformable microchannels. *Microfluid Nanofluid* **21** (4), 70.

SEO, J., WANG, C., CHANG, S., PARK, J., KIM, H.-Y. & KIM, W. 2019 A hydrogel-driven microfluidic suction pump with a high flow rate. *Lab on a Chip* **19** (10), 1790–1796.

SHIDHORE, T.C. & CHRISTOV, I.C. 2018 Static response of deformable microchannels: a comparative modelling study. *J. Phys.: Condens. Matter* **30** (5), 054002.

SOLTANE, H.B., ROIZARD, D. & FAVRE, E. 2013 Effect of pressure on the swelling and fluxes of dense PDMS membranes in nanofiltration: an experimental study. *J. Membr. Sci.* **435**, 110–119.

SQUIRES, T.M. & QUAKE, S.R. 2005 Microfluidics: fluid physics at the nanoliter scale. *Rev. Mod. Phys.* **77** (3), 977–1026.

TANAKA, T. & FILLMORE, D.J. 1979 Kinetics of swelling of gels. *J. Chem. Phys.* **70** (3), 1214–1218.

VAN DE VELDE, P., DERVAUX, J., DUPRAT, C. & PROTIÈRE, S. 2024 Imbibition and collapse between swelling fibres. *J. Fluid Mech.* **978**, A2.

VAN DE VELDE, P., FABRE-PARRAS, N., JOSSERAND, C., DUPRAT, C. & PROTIÈRE, S. 2023 Spreading and absorption of a drop on a swelling surface. *Europhys. Lett.* **144** (3), 33001.

VAN DE VELDE, P., MADKOUR, H., PROTIÈRE, S. & DUPRAT, C. 2025 Spreading on textiles: dynamics of drops on model poroelastic fibrous materials. *Phys. Rev. Fluids*. **10** (4), 040501.

WANG, X. & CHRISTOV, I.C. 2019 Theory of the flow-induced deformation of shallow compliant microchannels with thick walls. *Proc. R. Soc. A* **475** (2231), 20190513.

WANG, X. & CHRISTOV, I.C. 2021 Reduced models of unidirectional flows in compliant rectangular ducts at finite Reynolds number. *Phys. Fluids* **33** (10), 102004.

WEBBER, J.J. & WORSTER, M.G. 2023 A linear-elastic-nonlinear-swelling theory for hydrogels. Part 1. Modelling of super-absorbent gels. *J. Fluid Mech.* **960**, A37.

https://doi.org/10.1017/jfm.2026.11866 Published online by Cambridge University Press

XIA, Y. & WHITESIDES, G.M. 1998 Soft lithography. *Angew. Chem. Intl Ed. Engl.* **37** (5), 550–575.

XU, D., HEIL, M., SEEBÖCK, T. & AVILA, M. 2020 Resonances in pulsatile channel flow with an elastic wall. *Phys. Rev. Lett.* **125** (25), 254501.

YOON, J., CAI, S., SUO, Z. & HAYWARD, R.C. 2010 Poroelastic swelling kinetics of thin hydrogel layers: comparison of theory and experiment. *Soft Matt.* **6** (23), 6004–6012.

https://doi.org/10.1017/jfm.2026.11866 Published online by Cambridge University Press